Statistics and tensor analysis of polymer coil–stretch mechanism in turbulent drag reducing channel flow

Anselmo S. Pereira[1], **Gilmar Mompean**[1,†], **Laurent Thais**[1]
and Roney L. Thompson[2]

[1]Polytech'Lille and Laboratoire de Mécanique de Lille (LML), Université de Lille 1 – Sciences et Technologies, Cité Scientifique, 59655 Villeneuve d'Ascq, France

[2]COPPE, Department of Mechanical Engineering, Universidade Federal do Rio de Janeiro, Centro de Tecnologia, Ilha do Fundão, 21945-970, Rio de Janeiro, RJ, Brazil

The polymer coil–stretch mechanism in turbulent drag reducing flows is analysed using direct numerical simulations of viscoelastic finitely extensible nonlinear elastic fluids with the Peterlin approximation. The study is carried out taking into account low and high drag reduction regimes. The polymer stretching and the alignment between the conformation tensor and other relevant entities are investigated using statistical and tensor analysis. The significant alignment between the former and the velocity fluctuations product tensor indicates that the initial polymer stretching due to the mean shear is increased by the flow stress fluctuations, providing a supplementary polymer extension. In addition, interactions between the turbulence and the polymer are evaluated from an instantaneous turbulent energy exchange perspective by considering streamwise work fluctuating terms in elliptical and hyperbolic flow regions separately. Near the wall, polymers not only release energy to the streaks, but also to the elliptical (or vortical) and hyperbolic (or extensional) structures. However, polymers can also be dragged around near-wall vortices, passing through hyperbolic regions and experiencing a significant straining within both these turbulent structures and storing their energy. Hence, polymers weaken elliptical and hyperbolic structures leading to a tendency toward relaminarization of the flow. Polymer release of energy occurs primarily in the streamwise direction, which is in agreement with the enhanced streamwise velocity fluctuation observed in drag reducing flows. A detailed polymer coil–stretch mechanism is provided.

Key words: drag reduction, non-Newtonian flows, turbulence simulation

1. Introduction

The addition of a small amount of polymers of high molecular weight can lead to a pressure drop decrease in turbulent flows. Since the first observations reported by Forrest & Grierson (1931), Toms (1948) and Mysels (1949), numerous experimental

† Email address for correspondence: gilmar.mompean@polytech-lille.fr

studies have been conducted in attempts to make practical use of polymer-induced drag reduction (DR), including long-distance transport of liquids (Sellin *et al.* 1982), oil well operations (Burger & Chorn 1980), fire fighting (Fabula 1971), transport of suspensions and slurries (Golda 1986) and biomedical applications (Greene, Mostardi & Nokes 1980). In a remarkable and pioneering paper, Virk, Mickley & Smith (1967) performed a careful analysis with an experimental turbulent pipe flow apparatus and showed that if the friction drag for pipe flows is plotted in Prandtl–Kármán coordinates, it departs from the Prandtl–Kármán law (the onset of DR) to its bound, the so-called maximum drag reduction (MDR) or Virk's asymptote, as a result of an increase in either the Reynolds number, the polymer concentration or the polymer's molecular weight. Over the years, researchers have successfully analysed relevant aspects of this phenomenon and a significant literature is available, e.g. Hershey & Zakin (1967), Paterson & Abernathy (1970), Virk, Mickley & Smith (1970), Virk (1975), Bewersdorff (1982), Bewersdorff & Singh (1988), Moussa & Tiu (1994), Gyr & Tsinober (1995), Kalashnikov (1998). However, up to now, there has been no definitive consensus concerning the interactions between the turbulent energy and the deformations of the polymer.

Phenomenological explanations for polymer drag reduction gravitate around two major theories. According to the viscous theory, independently proposed by Lumley (1969) and Seyer & Metzner (1969) and supported by Ryskin (1987), polymer stretching in a turbulent flow produces an increase in the effective viscosity in a region outside of the viscous sublayer and in the buffer layer, which suppresses turbulent fluctuations, increasing the thickness of the buffer layer and reducing the wall friction. The elastic theory postulated by Tabor & de Gennes (1986) assumes that the elastic energy stored by the polymer becomes comparable to the kinetic energy in the buffer layer. Since the corresponding viscoelastic length scale is larger than the Kolmogorov scale, the usual energy cascade is inhibited, which thickens the buffer layer and reduces the drag (see also Joseph 1990).

Numerically, polymer-induced drag reduction theories have been intensively investigated for over a decade since the first simulations conducted by den Toonder, Nieuwstadt & Kuiken (1995) and Orlandi (1996). Using an inelastic generalized Newtonian fluid to analyse pipe (den Toonder *et al.* 1995) and channel (Orlandi 1996) flows, both researchers argued that DR seems to be closely related to the anisotropy of the elongational viscosity, a parameter that measures the resistance of the fluid against stretching deformations. Such an argument was also presented by Sureshkumar, Beris & Handler (1997), who performed the first self-consistent direct numerical simulation (DNS) of turbulent channel flow of a viscoelastic finitely extensible nonlinear elastic in the Peterlin approximation (FENE-P) fluid (Peterlin 1961), at a zero shear friction Reynolds number of 125. Their results suggest a partial suppression of turbulence within the buffer layer after the onset of drag reduction, which is linked with an enhanced effective viscosity attributed to the extension of polymers dispersed in the flow.

The explanations proposed in the three papers referred to above (den Toonder *et al.* 1995; Orlandi 1996; Sureshkumar *et al.* 1997) seem to corroborate Lumley's theory. In an attempt to quantify this viscous scenario, L'vov *et al.* (2004) used conservation principles to show that an additional effective viscosity growing linearly with the distance from the wall in the buffer layer has similar effects to those observed by the addition of flexible polymers in turbulent flows. This theoretical prediction was later confirmed by De Angelis *et al.* (2004), who performed a DNS of Newtonian turbulent flows with an added viscosity profile obtaining results previously observed

in viscoelastic FENE-P simulations. Additionally, using this simple linear viscosity model, De Angelis *et al.* (2004) were able to predict the maximum drag reduction asymptote, a point discussed in detail by Benzi *et al.* (2005).

It is important to note that the elastic theory has also been actively explored. Min *et al.* (2003) conducted a DNS of turbulent drag reducing channel flows in which the dilute polymer solution is simulated using the Oldroyd-B model. Their results showed good agreement with previous theoretical and experimental predictions of the onset of DR at specific friction Weissenberg numbers which is interpreted based on the elastic theory. Min *et al.* (2003) and Dallas, Vassilicos & Hewitt (2010) describe an elastic scenario in which the elastic energy stored in the near-wall region due to the uncoiling of polymer molecules is transported to and, to some extent, released in the buffer and log-law layers. This storage of energy around the near-wall vortices was confirmed by Dubief *et al.* (2004), who performed a DNS of turbulent polymer solutions in a channel using the FENE-P model, although, in contrast to Min *et al.* (2003) and Dallas *et al.* (2010), they proposed an autonomous regeneration cycle of polymer wall turbulence in which the coherent release of energy occurs in the very near-wall region, just above the viscous sublayer. In order to clarify the dynamics of the polymer–turbulence interaction, Thais, Gatski & Mompean (2012) used the DNS of a fully developed turbulent channel flow of Newtonian and viscoelastic FENE-P fluids at zero shear friction Reynolds numbers up to 1000 and carefully examined the budgets of turbulent kinetic energy and the elastic energy budget in drag reducing flows. The authors showed that the elastic energy production is small in the very near-wall region, growing with the distance from the wall and reaching a maximum value in the log-law region. This elastic energy production acts simultaneously as the dominant source of elastic energy and as the dominant sink of turbulent energy. This is rather in line with Tabor and De Gennes's description. However, recently, Thais, Gatski & Mompean (2013) emphasized that at $Re_{\tau_0} = 1000$, the elastic coupling between the turbulence and the polymer does not depend on the drag reduction regime (the level of viscoelasticity), which is in disagreement with the elastic theory.

Despite the discrepancies between the two most prominent theories, what seems to be in accordance with both scenarios is the relevance of the polymer coil–stretch process, which further imposes a transient behaviour on the drag reduction as well as a subsequent polymer degradation, a consequence of polymer elongation (Merrill & Horn 1984; Pereira, Andrade & Soares 2013; Soares *et al.* 2015). In order to understand the polymer coil–stretch process, Bagheri *et al.* (2012) presented direct numerical simulations of turbulent channel flow with passive Lagrangian linear (Oldroyd-B) and nonlinear (FENE) polymers. For the FENE model, the polymers are more elongated within the near-wall region although such extension becomes less heterogeneous as the Weissenberg number increases. Furthermore, a much stronger orientational trend is seen close to the wall, where the polymers are well aligned along the streamwise direction. The authors also verified the alignment of the end-to-end vector with respect to the principal directions of the rate-of-strain tensor and the vorticity vector. Nevertheless, they did not identify possible tensors capable of stretching the polymers, which would reveal more details about the uncoiling mechanism.

It is clear that the DR phenomenon is not completely understood and many aspects of the problem remain unclear. Any attempt to completely elucidate polymer-induced drag reduction must consider, at least, four important issues: the mechanism of polymer coil–stretch; the development of turbulent structures in viscoelastic flows; the exchange of energy between the turbulence and the polymers; and the breaking of the polymer molecules.

In the present paper, we investigate the polymer coil–stretch process with the aid of direct numerical simulations of the turbulent channel flow of a viscoelastic FENE-P fluid taking into account a wide range of zero shear friction Reynolds numbers (from 180 up to 1000). Tensorial and statistical analyses are developed in an attempt to highlight the role played by three relevant kinematic tensor entities in the polymer extension mechanism: the velocity fluctuation product tensor (which can be physically interpreted as an instantaneous Reynolds stress), the rate-of-strain tensor and the rate-of-rotation tensor. As the primary focus, the relative polymer stretch and the alignment between the conformation tensor and these three important tensor entities will be confronted. Additionally, joint probability density functions will be used in order to correlate the polymer–turbulence exchanges of energy and polymer orientations. Lastly, the flow will be divided into two distinct regions, following the *Q*-criterion of vortex identification (see Hunt, Wray & Moin 1988): an elliptical (or vortical) part where the second invariant of the velocity gradient tensor is positive and a hyperbolic (or extensional) part which is determined by the negative values of the second invariant of the velocity gradient tensor. The polymer work fluctuation will then be investigated within these regions, separately. The analyses that came out from these tools enable the proposition of a polymer coil–stretch mechanism based on the autonomous regeneration cycle reported by Dubief *et al.* (2004), which in turn was based on that conceived for Newtonian turbulent flows, previously presented by Jiménez & Pinelli (1999).

Following the description of the physical formulation and numerical methodology presented in § 2, our main results are separated into three parts: §§ 3–5. In the first part (§ 3), some classical time-averaged quantities are initially presented. In § 4, we analyse the distribution of polymer stretch across the wall distance, of which the effects on near-wall vortices and the dependence on L and Wi_{τ_0} are investigated as well, as exposed in § 4.1. Tensor analyses are conducted in § 4.2 in an attempt to verify the alignment between the conformation tensor and the other three relevant entities. In § 5, joint probability density functions are used in order to correlate the polymer–turbulence exchanges of energy and polymer alignments (§ 5.1). Additionally, the coil–stretch polymer process is linked with the coherent structures within the flow (§ 5.2). In § 6, these interactions are finally employed to describe a detailed cyclic mechanism of the polymer–turbulence interaction.

2. Physical formulation and numerical methodology

A turbulent channel flow of an incompressible dilute polymer solution is considered. Such a geometry is commonly adopted in direct numerical simulations due to its simplicity as well as its attractiveness for both experimental and theoretical studies of near-wall turbulent interactions. Here, the channel streamwise direction is $x_1 = x$, the spanwise direction is $x_2 = y$ and the direction normal to the wall is $x_3 = z$.

The instantaneous velocity field in the respective directions is $(u_x, u_y, u_z) = (u, v, w)$ and is solenoidal ($\nabla \cdot \boldsymbol{u} = 0$, where $\boldsymbol{u}$ denotes the velocity vector). The governing equations are scaled with the channel half-width, h, the bulk velocity, U_h, and the fluid density, ρ.

The scaled momentum equations are

$$\frac{\partial u_i}{\partial t} + u_j \frac{\partial u_i}{\partial x_j} = -\frac{\partial p}{\partial x_i} + \frac{\beta_0}{Re_h} \frac{\partial^2 u_i}{\partial x_j^2} + \frac{1}{Re_h} \frac{\partial \Xi_{ij}}{\partial x_j}. \quad (2.1)$$

In (2.1), p is the pressure, β_0 is the ratio of the Newtonian solvent kinematic viscosity (ν_N) to the total zero shear kinematic viscosity ($\nu_0 = \nu_N + \nu_{p0}$) and the bulk Reynolds

number is $Re_h = U_h h/\nu_0$. The extra stress tensor components are denoted by $\varXi_{ij}$. The formalism of (2.1) includes the assumption of a homogeneous polymer concentration which is governed by the viscosity ratio β_0, where $\beta_0 = 1$ yields the limiting behaviour of the Newtonian case.

The extra stress tensor components ($\varXi_{ij}$) in (2.1) represent the polymer's contribution to the stress of the solution. This contribution is accounted for by a single spring–dumbbell model. We employ here the FENE-P kinetic theory (Bird, Armstrong & Hassager 1987), which is the most preferred one due to its physically realistic finite extensibility of the polymer molecules and to its relatively simple second-order closure. This model employs the phase-averaged conformation tensor, $\boldsymbol{C}$. The components of the extra stress tensor are then

$$\varXi_{ij} = \frac{(1 - \beta_0)}{Wi_h}(f\{\text{tr}(\boldsymbol{C})\}C_{ij} - \delta_{ij}), \tag{2.2}$$

in which $Wi_h = \lambda U_h/h$ is the bulk Weissenberg number (λ being the relaxation time scale), δ_{ij} is the Kronecker delta operator and $f\{\text{tr}(\boldsymbol{C})\}$ is given by the Peterlin approximation

$$f\{\text{tr}(\boldsymbol{C})\} = \frac{L^2 - 3}{L^2 - \text{tr}(\boldsymbol{C})}, \tag{2.3}$$

where L is the maximum polymer molecule extensibility and $\text{tr}(\cdot)$ represents the trace operator. The governing equation for the conformation tensor are

$$\frac{\partial C_{ij}}{\partial t} + u_k \frac{\partial C_{ij}}{\partial x_k} - \frac{\partial u_i}{\partial x_k}C_{kj} - \frac{\partial u_j}{\partial x_k}C_{ki} + \frac{f(\text{tr}(\boldsymbol{C}))C_{ij} - \delta_{ij}}{Wi_h} = \left(\frac{1}{Sc_c Re_h}\right)\frac{\partial^2 C_{ij}}{\partial x_k^2}, \tag{2.4}$$

in which $Sc_c = \nu_0/\kappa_c$ is the Schmidt number defined as the ratio of the total kinematic zero shear rate viscosity (ν_0) to an artificial stress diffusivity κ_c. This explicit elliptic diffusion term included in (2.4) is an artefact used to improve numerical stability in pseudo-spectral simulations of viscoelastic fluids. This dissipative term was first introduced in this context by Sureshkumar & Beris (1995), and the methodology was subsequently validated under a variety of flows and material parameters (see Housiadas & Beris 2003).

Since the numerical scheme for DNS was already given in detail by Thais *et al.* (2011), we present here a brief description of the mathematical and numerical approaches. The hybrid MPI/OPENMP algorithm used was tailored to run properly in massively parallel architectures. The hybrid spatial scheme includes Fourier spectral accuracy in the two homogeneous directions (x and y) and sixth-order compact finite differences for the first- and second-order wall-normal derivatives (z direction). Time marching can be up to fourth-order accurate by the use of the Adams–Moulton scheme for the viscous terms and Adams–Bashforth for the explicit terms. Pressure–velocity coupling is facilitated by a higher-order generalization of the semi-implicit fractional step method on a non-staggered grid arrangement analysed by Armfield & Street (2000). In order to attenuate high wavenumber energy accumulation, de-aliasing and fourth-order filtering are performed in the two homogeneous and wall-normal directions, respectively.

The parameters for the turbulent Newtonian and FENE-P channel flows studied here are summarized in table 1. Our simulated cases were chosen keeping in mind that viscoelastic fluids can have significantly different statistical behaviour from a

$Re_{\tau 0}$	$We_{\tau 0}$	L	β	$N_x \times N_y \times N_z$	$\Delta_x^+ \times \Delta_y^+ \times \Delta_{z,min}^+$	$\Delta_{z,max}^+$	DR (%)
180	0	0	1	$512 \times 128 \times 129$	$8.8 \times 6.6 \times 0.2$	7.1	0
180	50	30	0.9	$512 \times 128 \times 129$	$8.8 \times 6.6 \times 0.2$	7.1	28.5 (LDR)
180	115	30	0.9	$512 \times 128 \times 129$	$8.8 \times 6.6 \times 0.2$	7.1	38.4 (LDR)
180	50	100	0.9	$512 \times 128 \times 129$	$8.8 \times 6.6 \times 0.2$	7.1	47.0 (HDR)
180	115	100	0.9	$512 \times 128 \times 129$	$8.8 \times 6.6 \times 0.2$	7.1	62.3 (HDR)
395	0	0	1	$1024 \times 256 \times 257$	$9.7 \times 7.3 \times 0.2$	7.9	0
395	115	100	0.9	$1024 \times 256 \times 257$	$9.7 \times 7.3 \times 0.2$	7.9	62.0 (HDR)
590	0	0	1	$1536 \times 512 \times 257$	$9.7 \times 5.4 \times 0.5$	10.4	0
590	115	100	0.9	$1536 \times 512 \times 257$	$9.7 \times 5.4 \times 0.5$	10.4	61.0 (HDR)
1000	0	0	1	$1536 \times 768 \times 385$	$12.3 \times 6.1 \times 0.5$	12.1	0
1000	115	100	0.9	$1536 \times 768 \times 385$	$12.3 \times 6.1 \times 0.5$	12.1	58.0 (HDR)

TABLE 1. Parameters for the DNS of Newtonian and FENE-P turbulent channel flows.

Newtonian fluid. For a given turbulence level, as parametrized by the zero shear friction Reynolds number $Re_{\tau 0}$ (defined as $Re_{\tau 0} = u_\tau h / \nu_0$, where u_τ denotes the friction velocity), this effect can vary with the friction Weissenberg number, $Wi_{\tau 0}$ (where $Wi_{\tau 0} = \lambda u_\tau^2 / \nu_0$) and the maximum polymer extension length, L. In this paper, four Newtonian flows and seven viscoelastic flows were examined, keeping the viscosity ratio β_0 fixed at 0.9 and taking into account four different values of the zero shear friction Reynolds number ($Re_{\tau 0} = 180$, $Re_{\tau 0} = 395$, $Re_{\tau 0} = 590$ and $Re_{\tau 0} = 1000$) and two different values of the friction Weissenberg number and the maximum polymer molecule extensibility ($Wi_{\tau 0} = 50$; $Wi_{\tau 0} = 115$; $L = 30$; $L = 100$), which provided drag reduction regimes from 28.5 % up to 62.3 %.

The simulations were conducted at constant pressure gradient, leaving the mass flow rate of non-Newtonian flows to increase and then oscillate about a steady state characterized by a new time-averaged Reynolds number, Re_h. The drag reduction is evaluated as

$$DR = 1 - \mu_w^{2(1-n)/n} \left(\frac{Re_{h,NEWT}}{Re_h} \right)^{(2/n)}, \qquad (2.5)$$

where

$$\mu_w = \left(\frac{2Re_{\tau 0}\beta_0}{2Re_{\tau 0} + 1 - \beta_0} \right) \langle \tau_w \rangle \qquad (2.6)$$

accounts for the shear-thinning property of the FENE-P model (Housiadas & Beris 2004). In this expression, $Re_{h,NEWT}$ is the bulk Reynolds number related to the corresponding Newtonian case (the Newtonian case at the same $Re_{\tau 0}$), $< \tau_w >$ denotes the area-averaged wall shear stress and $n = 1.14286$ is the exponent of the Dean correlation, which relates the bulk and friction Reynolds numbers for Newtonian turbulent channel flow (Dean 1978). Time averaging of DNS data is taken in time over some 500 flow snapshots spanning several eddy turnover times, while spatial averaging (indicated by '$\langle \rangle$') is taken in the two homogeneous channel directions (x, y).

Two drag reducing regimes are shown in table 1: the high drag reduction (HDR; $DR > 40$ %) regime and the low drag reduction (LDR; $DR \leqslant 40$ %) regime. Physically,

the main difference between these two regimes consists in the fact that for LDR flows, the Reynolds stresses play a major role, whereas in the HDR regime, the near-wall dynamics of the flow is dominated by the polymer stresses (White & Mungal 2008).

The channel extent for the flow cases at Re_{τ_0} up to of 590 was $Lx \times Ly \times Lz = 8\pi \times 1.5\pi \times 2.0$. For the highest zero shear friction Reynolds number flow, $Lx \times Ly \times Lz = 6\pi \times 1.5\pi \times 2.0$. The number of mesh points ($Nx \times Ny \times Nz$) shown in table 1 for each case corresponds to a grid resolution of $8.8 \leqslant \Delta x^+ \leqslant 12.3$, $5.4 \leqslant \Delta y^+ \leqslant 7.3$, and $0.2 \leqslant \Delta z^+ \leqslant 12.1$. The superscript '+' indicates normalization by the friction velocity, defined by $u_\tau = \sqrt{\tau_w/\rho}$, and the total kinematic zero shear rate viscosity. The Schmidt number $Sc_c = 0.1$ was necessary to keep the algorithm stable and the conformation tensor symmetric positive definite.

3. Statistics of the flow

3.1. *Time-averaged statistics*

The distributions of the mean velocity in wall coordinates, $\langle \overline{U_x}^+ \rangle$, for turbulent channel flows of Newtonian and viscoelastic solutions are displayed in figure 1(*a*). The bar indicates the time average and '$\langle \rangle$' denotes the *x*–*y* plane average. The grey circles represent the Newtonian mean velocity profile at $Re_{\tau_0} = 180$ while the other symbols represent the viscoelastic flows. In the viscous sublayer ($0 < z^+ < 5$), where the total stress is predominantly associated with viscous effects, the mean velocities converge to the same linear shape $\langle \overline{U_x}^+ \rangle = z^+$ represented by the solid grey line. As the wall distance increases, the Reynolds stress becomes important and comparable to the viscous stress within the Newtonian buffer layer ($5 < z^+ < 30$). Then, the Newtonian mean velocity departs quickly from the linear profile, taking on a logarithmic dependence on z^+ (grey dashed line) in the Newtonian log-law region, $z^+ > 30$, $\langle \overline{U_x}^+ \rangle = (1/\kappa) \ln(z^+) + A_1$ where κ is commonly called the von Kármán coefficient ($1/\kappa$ is the slope) and A_1 is the intercept at $z^+ = 1$. For Newtonian channel flows over a hydraulically smooth wall, $\kappa = 0.4$ and $A_1 = 5.5$ (Kim, Moin & Moser 1987). In order to better describe our results, we use the boundaries of the viscous sublayer, the buffer layer and the log-law Newtonian regions to define regions I, II and III, respectively. It is important to emphasize, however, that regions II and III do not necessarily represent the buffer layer and the log-law region for the viscoelastic cases, since the polymers can increase the former layer, reducing the latter.

The interactions between the viscoelastic fluid dynamics and the turbulent flow dynamics result in changes in the mean velocity profile relative to the Newtonian fluid. The polymer drag reduction phenomenon leads to an increased bulk mean velocity, as observed by comparing the viscoelastic profiles plotted in figure 1. When a high enough polymer concentration is used, the maximum level of drag reduction (MDR) is attained. In that state, the velocity profile is commonly represented by the Virk's asymptote (Virk *et al.* 1970), $\langle \overline{U_x}^+ \rangle = 11.7 \ln(z^+) + 17.8$ which is a matter of recent controversy (White, Dubief, & Klewicki 2012). Experimental and recent numerical results based on DNS (Escudier, Presti & Smith 1999; Ptasinski *et al.* 2001; Escudier, Nickson, & Poole 2009; Thais *et al.* 2012) indicate a parallel upward shift of the logarithmic region of the mean velocity profile with increasing DR, which is clearly perceived at high Reynolds numbers (see Thais *et al.* 2013). Such a behaviour suggests a significant extension of the buffer layer region into the channel caused by the polymers. For viscoelastic fluids, the cross-over to a presumed Newtonian plug flow occurs at a distance from the wall where the Reynolds stress momentum flux
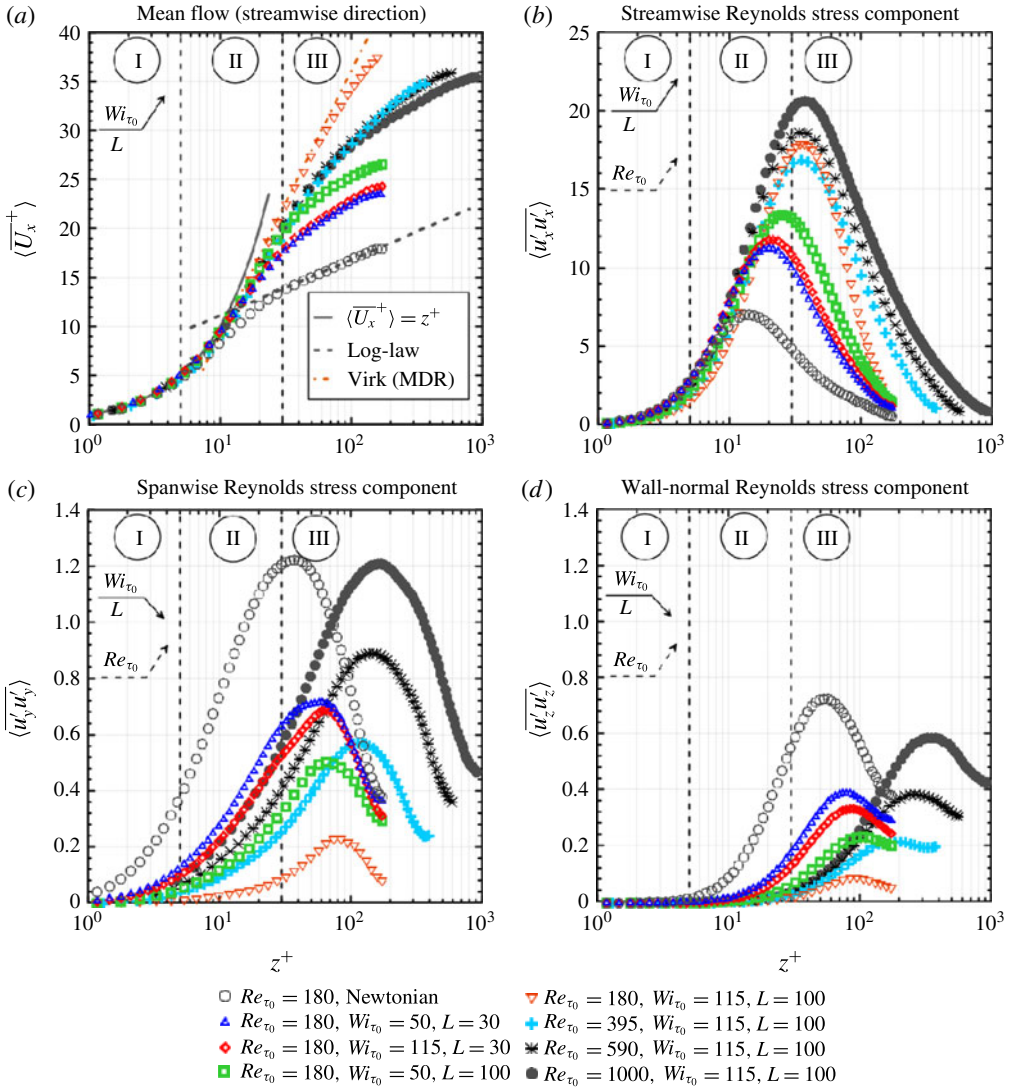
FIGURE 1. (Colour online) Mean velocity profiles in the streamwise direction (*a*), $\langle \overline{U_x}^+ \rangle$, and normal components of the Reynolds stress (*b–d*) for Newtonian and viscoelastic channel flows, against the normalized wall distance.

is no longer negligible compared to that of the polymer/viscous stress. Figure 1(*b–d*) show the normal components of the Reynolds stress tensor, whose components are defined as the time average of the velocity fluctuation product ($\overline{u_i' u_j'}^+$). The mean effect of the polymer on the turbulence is anisotropic and induces an increase in the streamwise normal Reynolds stress component (figure 1*b*), while weakening both the spanwise (figure 1*c*) and the wall-normal (figure 1*d*) terms, as experimentally found by many researchers such as Pinho & Whitelaw (1990), Warholic, Massah & Hanratty (1999) and White, Somandepalli & Mungal (2004). This effect is more pronounced as the elasticity increases, as indicated by the solid black arrows. In the most elastic flow at $Re_{\tau_0} = 180$ (orange inverted triangles), for instance, the peak
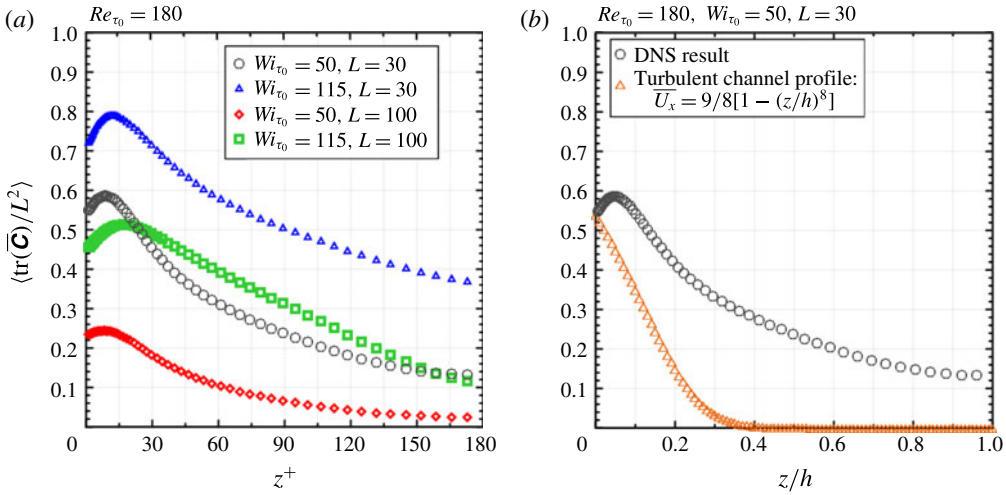
FIGURE 2. (Colour online) (*a*) Evolution of the mean relative polymer extension, $\langle \text{tr}(\overline{\boldsymbol{C}})/L^2 \rangle$, against the normalized wall distance. (*b*) Effects of mean shear stress profile on polymer extension.

of $\langle \overline{u'_x u'_x}^+ \rangle$ moves from $z^+ \approx 12$ (region II) to $z^+ \approx 32$ and its value is one order of magnitude greater than the Newtonian one (grey open circles). In addition, the other components also shift away from the wall, but their peaks decrease by one order of magnitude compared to the Newtonian flow. Since vortices produce significant transverse fluctuations, the reduction of both u'_y and u'_z suggests a strong interaction between these intermittent structures and polymers (Dubief *et al.* 2004). Lastly, the dashed arrows indicate that the normal Reynolds stress components are an increasing function of Re_{τ_0}. Their peaks move towards the channel centre with increasing Reynolds number.

The variations in polymer mean stresses across the channel can be highlighted by analysing the polymer mean stretch, which is linked with the former by the Peterlin function (2.3). The distribution of the relative polymer mean stretch $\langle \text{tr}(\overline{\boldsymbol{C}})/L^2 \rangle$ as a function of z^+ is displayed in figure 2(*a*), for all viscoelastic cases studied in the present paper. As a common point, the polymer molecules exhibit a significant extension at the wall, which increases in the buffer layer, where its peak is attained. This peak magnitude, as well as its location, is a decreasing function of L, but increases with increasing Wi_{τ_0} (these trends are discussed in § 4.1). As the wall distance increases further, $\langle \text{tr}(\overline{\boldsymbol{C}})/L^2 \rangle$ becomes less pronounced until achieving its minimum level at $z^+ = 180$. A very simple method to clarify the polymer stretching mechanism consists in solving (2.4) using different mean velocity profiles. The result is illustrated in figure 2(*b*), where the less elastic flow is considered (grey open circles), as well as the polymer extension produced in this fluid by a turbulent-channel-like velocity profile $\overline{U_x} = (9/8)[1 - (z/h)^8]$ (Dallas *et al.* 2010). As the derivative of the mean velocity with respect to the wall-normal direction increases, the polymers stretch considerably, due to the increase of the shear stress. More specifically, the profile of $\langle \text{tr}(\overline{\boldsymbol{C}})/L^2 \rangle$ follows the mean viscous shear stress feature. Comparing the relative polymer extensions obtained from a turbulent-like mean velocity profile (orange inverted triangles) and DNS results (grey open circles), it is interesting to observe that both curves depart from the same level (≈ 0.54), at $z^+ = 0$.

However, as the wall distance increases, the discrepancy between them becomes pronounced. In fact, near the wall, the increasing $\langle \mathrm{tr}(\overline{\boldsymbol{C}})/L^2 \rangle$ noticed for the grey circles curve suggests that in this region there is a particular flow topology capable of producing an increase in the polymer extension beyond the viscous mean shear level represented by the orange inverted triangles. In other words, the viscous mean stress is responsible for a relevant polymer stretching, which is incremented since the turbulent structures interact with the polymer molecules, providing a supplementary polymer extension. We believe these intermittent polymer–turbulence interactions are also responsible for the polymer coil–stretch process, which will be analysed in later subsections from statistical and tensorial perspectives.

All the trends discussed above considering $Re_{\tau_0} = 180$ are also observed at higher zero shear friction Reynolds numbers, as previously reported by Thais *et al.* (2012) and Thais *et al.* (2013).

4. Polymer stretching and alignment

In order to analyse the effects of instantaneous polymer stretching on the flow, the following data and results were evaluated at the same instant of simulation, after a statistical steady state was achieved. Such an instantaneous analysis is justified by the fact that in turbulent flows, the polymer action is likely to be as intermittent as the near-wall vortices (see Dubief *et al.* 2004). Hence, these intermittent events may be hidden by a time-averaging procedure. In other words, such an analysis of the instantaneous quantities could reveal less expressive but important events for the DR phenomenon.

Although in this subsection we analyse the effects of the elasticity on the stretching and alignment of the polymers at a low zero shear friction Reynolds number, $Re_{\tau_0} = 180$, it is important to emphasize that the trends shown below are observed for all viscoelastic cases studied. In other words, the physical aspects of DR discussed here are not affected by low Reynolds number effects.

4.1. *Polymer stretching*

The three-dimensional structures shown in figure 3 represent the isosurfaces of the vortical regions, defined as the positive second invariant of the velocity gradient tensor, $\nabla \boldsymbol{u}$, in Newtonian (*a*) and viscoelastic (*b–e*) flows. For incompressible flows, the second invariant of $\nabla \boldsymbol{u}$, Q, can be used to identify vortical structures, the so-called Q-criterion (see Hunt *et al.* 1988), and simplified as

$$Q = \tfrac{1}{2}(\|\boldsymbol{W}\|^2 - \|\boldsymbol{D}\|^2) > 0, \tag{4.1}$$

which indicates the spatial regions where the Euclidean norm of the rate-of-rotation tensor, $\|\boldsymbol{W}\|$, dominates that of the rate of strain, $\|\boldsymbol{D}\|$ (the Euclidean norm of a generic second-order tensor $\boldsymbol{A}$ is $\|\boldsymbol{A}\| = \sqrt{\mathrm{tr}(\boldsymbol{A} \cdot \boldsymbol{A}^T)}$). These structures follow an organized hierarchy across the channel. In the vicinity of the wall ($z^+ < 20$), eddies are found to be pairs of counter-rotating quasi-streamwise vortices, while for $z^+ > 30$, these eddies resemble hairpins (the so-called horseshoe vortices). The formation of such morphologies is induced by combined second-quadrant ejection ($u'_x < 0$, $u'_z > 0$; Q2 event) and fourth-quadrant sweep ($u'_x > 0$, $u'_z < 0$; Q4 event) events within the flow (see Adrian 2007). Specifically, the hairpin vortices are composed of three well defined parts. The legs are regions of rotation quasi-aligned with the streamwise direction. The head is a rotation part aligned with the spanwise direction. The necks
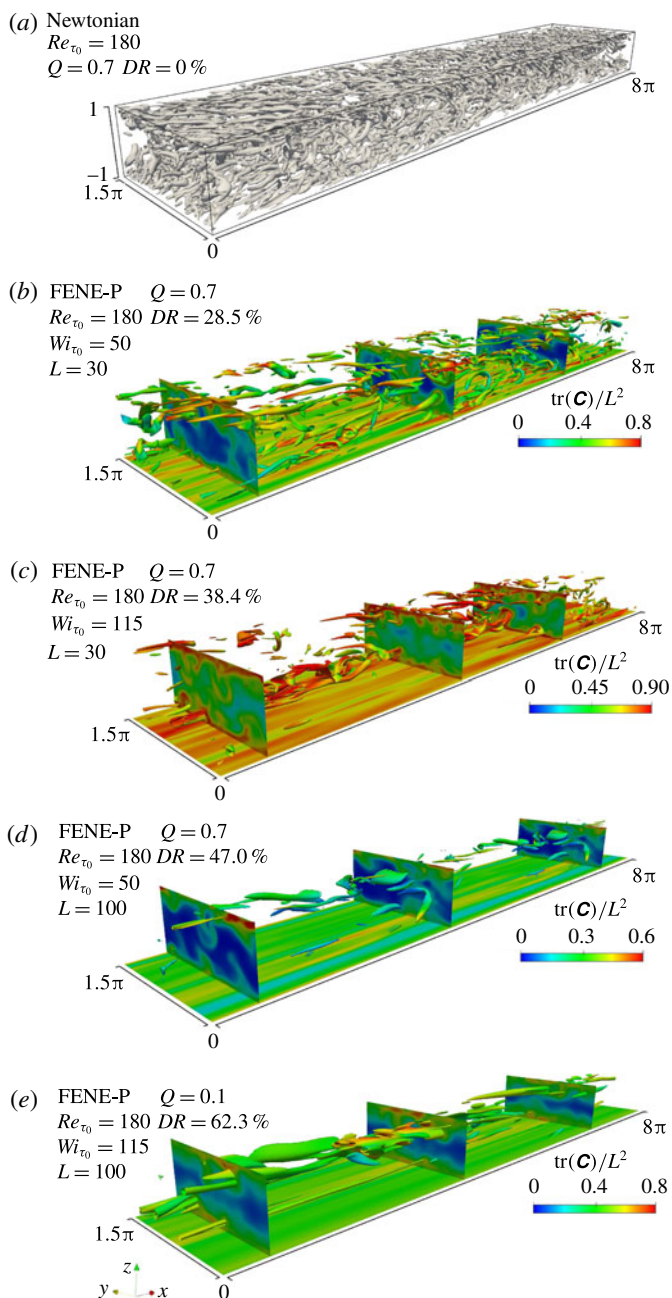
FIGURE 3. (Colour online) The three-dimensional structures represent isosurfaces of vortical regions defined as a positive value of the second invariant of velocity gradient tensor, ∇u. The colours indicate the polymer stretching, $\mathrm{tr}(C)/L^2$.

are the connections between the legs and the head of the hairpin. These three parts, as well as the velocity fluctuations associated with them, can be seen in detail in figure 4, where a typical hairpin extracted from our less elastic flow ($Re_{\tau_0} = 180$, $Wi_{\tau_0} = 50$ and $L = 30$) is coloured by the Q events.
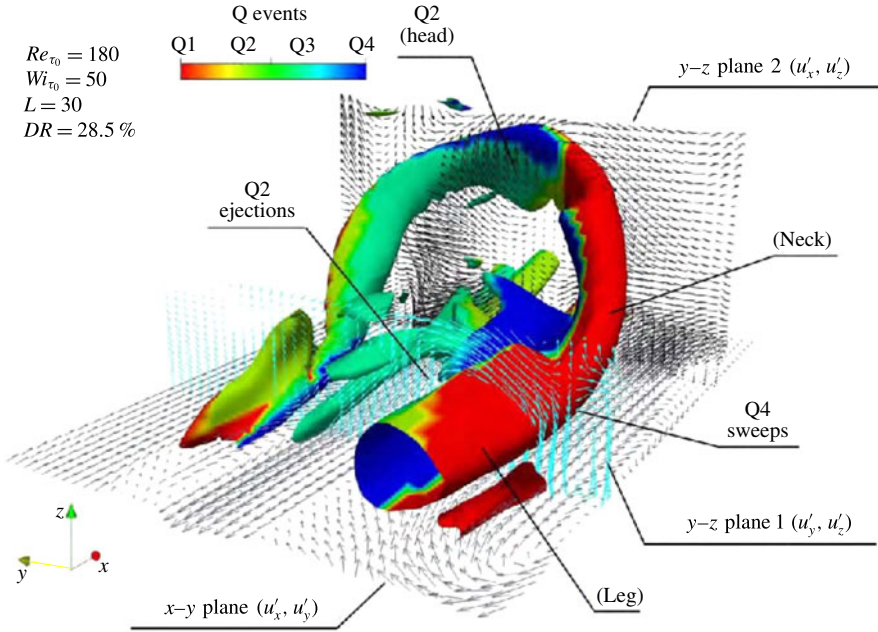
FIGURE 4. (Colour online) Typical hairpin extracted from a viscoelastic flow ($Re_{\tau_0} = 180$; $Wi_{\tau_0} = 50$; $L = 30$) with $Q = 0.7$ and coloured by the Q1 ($u_x' > 0$, $u_z' > 0$), Q2 ($u_x' < 0$, $u_z' > 0$), Q3 ($u_x' < 0$, $u_z' < 0$) and Q4 ($u_x' > 0$, $u_z' < 0$) events.

Comparing figure 3(*a–e*), it can be seen that the number of vortices with a value of the *Q*-criterion equal to 0.7 decreases with increasing elasticity (*We* and *L*). For $Wi_{\tau_0} = 115$ and $L = 100$, which provides $DR = 62.3\%$, the vortices with $Q = 0.7$ are completely gone and the vortices with $Q = 0.1$ (figure 3*e*) are only found close to the walls. In viscoelastic flows, the vortical structures are significantly weaker than in the Newtonian flow, which is considered fundamental evidence of the polymer–turbulence interactions and the consequent drag reduction (Terrapon *et al.* 2004; Kim *et al.* 2007, 2008; White & Mungal 2008). As the elasticity increases, some characteristics of the vortices change: their thicknesses and streamwise lengths increase, while their strengths weaken, which is clearly observed by comparing figure 3(*a,e*). Furthermore, the vortices become more parallel to the wall. In the log-law region, the hairpin head is strongly weakened. It has been experimentally and numerically shown that in drag reducing flows, the streamwise component of the Reynolds normal stresses increases relative to the Newtonian case, while the other components of the Reynolds stress tensors decrease (Wei & Willmarth 1992; Warholic *et al.* 1999; Ptasinski *et al.* 2001; Kim *et al.* 2007; Thais *et al.* 2012). These variations seem to be closely connected with the coil–stretch polymer transition and the consequent vortex structural changes (Dimitropoulos *et al.* 2005). The colours in figure 3(*b–e*) indicate the relative polymer stretch, tr($\mathbf{C}$)/L^2. The *y–z* planes show that for all four viscoelastic flows, the polymers are more stretched close to the wall (yellow and red regions). In contrast, the polymer extensions are less pronounced in the middle of the channel (blue regions). The isosurface colours and those of the intersections between vortical structures and *y–z* planes show that the polymers are more extended around the near-wall vortices.
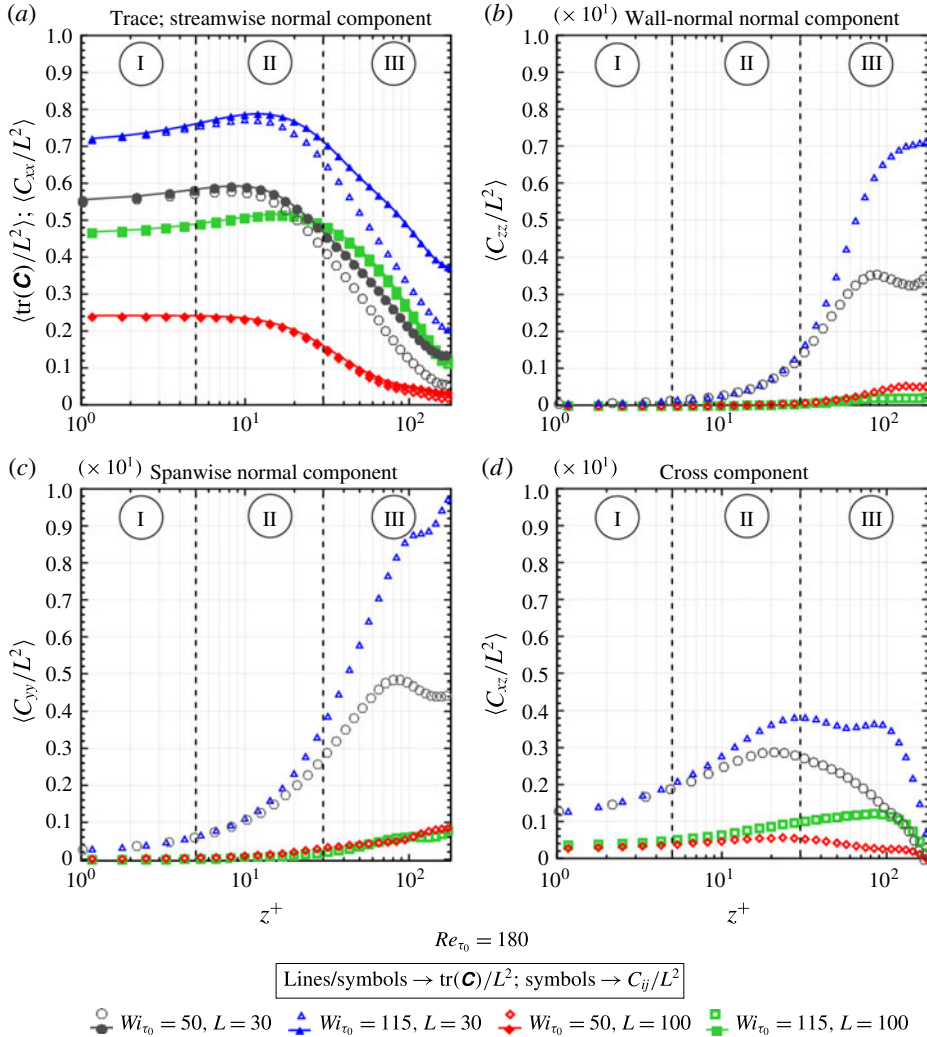
FIGURE 5. (Colour online) Normalized conformation tensor as a function of the normalized wall distance. Streamwise normal components of $\boldsymbol{C}$ and $\mathrm{tr}(\boldsymbol{C})/L^2$ (open and solid in a, respectively). Spanwise normal component of $\boldsymbol{C}$ (b). Wall-normal component of $\boldsymbol{C}$ (c). Cross-components (d).

The stretching of the polymers can be seen more clearly in figure 5(a), where the evolution of the x–y-plane-averaged normalized trace of the instantaneous conformation tensor, $\langle\mathrm{tr}(\boldsymbol{C})/L^2\rangle$, is plotted against the wall distance z^+ (solid symbols) together with the normalized streamwise normal component of the conformation tensor, $\langle C_{xx}/L^2\rangle$ (open symbols). The percentage of polymer extension, $\langle\mathrm{tr}(\boldsymbol{C})/L^2\rangle$, is relatively high at the wall, achieving a peak in the very near-wall region ($z^+ < 20$), the exact location of which varies with L and Wi_{τ_0}. This peak is commonly associated with the streamwise vortices (see Dubief *et al.* 2004; Dimitropoulos *et al.* 2005; Dallas *et al.* 2010). After this point, $\langle\mathrm{tr}(\boldsymbol{C})/L^2\rangle$ starts to decrease, until reaching its minimum at the channel centre. In comparing the grey solid circles with the red solid diamonds, or the blue solid triangles with the green solid squares, it can be clearly seen that

$\langle \text{tr}(\textbf{\textit{C}})/L^2 \rangle$ decreases with increasing L, for fixed Re_{τ_0} and Wi_{τ_0}, which suggests that the large polymer molecules could be less susceptible to chain scission degradation (Pereira & Soares 2012). A further comparison of the grey solid circles with the blue solid triangles, or of the red solid diamonds with the green solid squares, reveals that the relative polymer extension becomes greater as the friction Weissenberg number increases, since higher values of the polymer time scale induce the polymer molecules to be influenced by a wider spectrum of time scales of the flow (Dallas *et al.* 2010). Figure 5(*a*) also shows that the dominant contribution to the trace of the conformation tensor comes from C_{xx}, i.e. $\langle \text{tr}(\textbf{\textit{C}})/L^2 \rangle \approx \langle C_{xx}/L^2 \rangle$ (especially near the wall and for the highest value of L, $L = 100$). This distribution suggests a significant stretching of the polymers in the streamwise direction. The other component with a non-zero wall value is the off-diagonal component C_{xz}, normalized and displayed in figure 5(*d*). However, its value at the wall is almost two orders of magnitude smaller than that of the C_{xx} component. Moreover, as Wi_{τ_0} and L increase, the profile of $\langle C_{xz}/L^2 \rangle$ follows the same tendencies noted in figure 5(*a*), reaching its peaks at z^+ not much different from those observed for C_{xx}. The peak magnitude of the off-diagonal component C_{xz} is comparable to that of the C_{zz} component (plotted in figure 5*b*), although both are only slightly smaller than the peak magnitude of the C_{yy} component (shown in figure 5*c*). It is worth noting that $\langle C_{xz}/L^2 \rangle$ is an increasing function of the molecular relaxation time (the variations of which are here computed by changing Wi_{τ_0} at fixed Re_{τ_0}) although a saturation effect is observed when increasing the elasticity (the red diamonds and green square curves are close). This saturation effect is also seen for C_{zz} (figure 5*b*) and C_{yy} (figure 5*c*). The peak magnitude of the normal components C_{zz} and C_{yy} are both one order of magnitude smaller than that of the C_{xx} component, starting with a zero wall value. Lastly, as Wi_{τ_0} increases, C_{zz} and C_{yy} increase. The opposite behaviour is observed with increasing L. These two normal components exhibit maximum values within region III ($60 < z^+ < 90$), as previously reported by Thais *et al.* (2012), which is currently linked to the straining flows around the vortices (Dubief *et al.* 2004; Dimitropoulos *et al.* 2005).

In figure 5, it is worth noting that $C_{xx} \gg C_{yy} > C_{zz} \approx C_{xz}$ indicates a strong anisotropic behaviour of the conformation tensor. This anisotropy seems to dramatically influence the statistics of the fluctuating velocity fields, especially at small scales. The analysis of the trace of the conformation tensor reveals two locations of interest that will be systematically explored in this paper: $z^+ = 8.2$, the approximate position where $\langle \text{tr}(\textbf{\textit{C}})/L^2 \rangle$ is a maximum; $z^+ = 180$, where the trace of the conformation tensor reaches its minimum value with respect to L^2.

4.2. *Polymer alignment*

Figure 6 shows the average values in the x–y plane of the cosines of the angles Ψ between the first principal direction, e_1, of our three relevant tensor entities (the eigenvector related to the largest eigenvalue) and the three unit vectors e_x (streamwise; figure 6*a*), e_y (spanwise; figure 6*b*) and e_z (wall normal; figure 6*c*) against the normalized wall distance, for the Newtonian case.

The alignment between the first principal direction of the velocity fluctuation product tensor, $\boldsymbol{\tau}'$ (whose components are defined by $u_i' u_j'$), and e_x, indicated in figure 6(*a*) by the blue open triangles, is accentuated near the wall, growing within the buffer layer, where $\langle \cos \Psi(e_1^{\tau'}, e_x) \rangle$ achieves its peak magnitude (≈ 0.85) at $z^+ \approx 8.2$. This is consistent with the fact that $u_x' u_x'$ is the most important component of $\boldsymbol{\tau}'$ in the near-wall region. However, as the wall distance increases, $u_y' u_y'$, $u_z' u_z'$ and $u_x' u_z'$ become
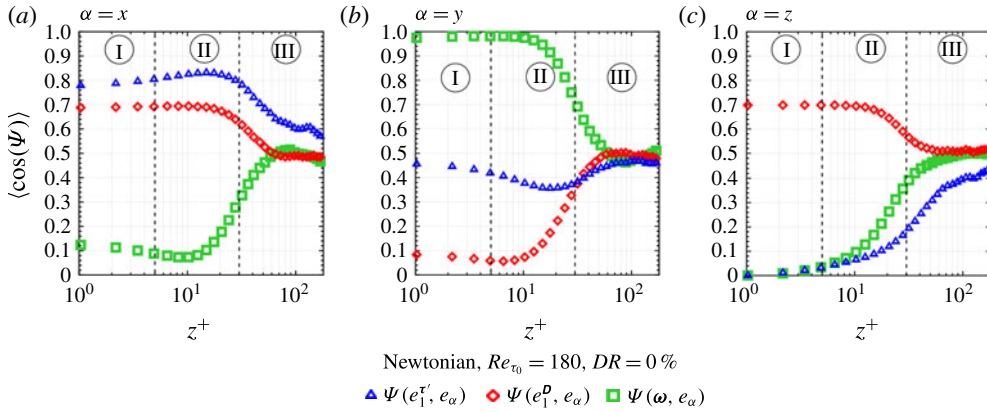
FIGURE 6. (Colour online) Average values in the x–y plane of the cosines of the angles between the principal directions of a given tensor and the three unit vectors e_x, e_y and e_z (which represent the streamwise, spanwise and wall-normal directions) against the normalized wall distance.

important while $u'_x u'_x$ decreases, considerably reducing $\langle \cos \Psi (e_1^{\tau'}, e_x) \rangle$ in the middle of the channel (≈ 0.57). A different behaviour is observed by analysing the angles between $e_1^{\tau'}$ and both the spanwise and wall-normal directions as functions of z^+, as shown in figures 6(*b*) and 6(*c*), respectively. Firstly, at the wall, $\langle \cos \Psi (e_1^{\tau'}, e_y) \rangle \approx 0.48$ while $\langle \cos \Psi (e_1^{\tau'}, e_z) \rangle = 0$. Although an increase in $\langle \cos \Psi (e_1^{\tau'}, e_z) \rangle$ with z^+ is noted, the buffer layer favours the alignment between τ' and the streamwise direction. Consequently, $\langle \cos \Psi (e_1^{\tau'}, e_y) \rangle$ decreases, reaching a minimum value of 0.37 at $z^+ \approx 15$. Lastly, in the middle of the channel, both $\langle \cos \Psi (e_1^{\tau'}, e_y) \rangle$ and $\langle \cos \Psi (e_1^{\tau'}, e_z) \rangle$ are approximately 0.5, indicating a random tendency of the alignment of τ' with both the y and z directions.

The orientation of the rate-of-strain tensor presented in figure 6(*a*–*c*) exhibits an interesting behaviour as the wall distance increases. Since in the viscous sublayer the Reynolds stress tensor is negligible compared to the viscous stress tensor (Dubief *et al.* 2004), the flow in this region is laminar and, consequently, $\langle \cos \Psi (e_1^D, e_x) \rangle \approx \sqrt{2}/2$, $\langle \cos \Psi (e_1^D, e_y) \rangle \approx 0$, and $\langle \cos \Psi (e_1^D, e_z) \rangle \approx \sqrt{2}/2$. In contrast, in the log-law region, the flow is driven by the turbulence, and $\langle \cos \Psi (e_1^D, e_x) \rangle \approx \langle \cos \Psi (e_1^D, e_y) \rangle \approx \langle \cos \Psi (e_1^D, e_z) \rangle \approx 0.5$, which emerges from a weak velocity gradient, of which the tendency of direction is not clear.

The green open squares in figure 6(*a*–*c*) show the orientation of the vorticity vector. Following the rate-of-strain tensor, beyond the buffer layer ($60 < z^+ < 180$), a chaotic alignment is perceived, since $\langle \cos \Psi (\boldsymbol{\omega}, e_x) \rangle = \langle \cos \Psi (\boldsymbol{\omega}, e_y) \rangle = \langle \cos \Psi (\boldsymbol{\omega}, e_z) \rangle \approx 0.5$. However, close to the wall ($z^+ < 20$), the vorticity vector tends to be strongly aligned with the spanwise direction.

Following the method described above, the effects of a polymer on the average orientation of our three relevant tensor entities are plotted against the wall distance in figures 7 and 8 for two drag reduction regimes: the less elastic ($DR = 28.5\%$, $Wi_{\tau_0} = 50$ and $L = 30$) and the most elastic ($DR = 62.3\%$, $Wi_{\tau_0} = 115$ and $L = 100$). In this subsection, we use the acronyms LDR and HDR to refer to these two cases. The orientation of the conformation tensor is also considered.

The polymer alignment in the LDR case is shown in figure 7(*a*–*c*). The grey open symbols indicate that in the viscous sublayer, the conformation tensor is well
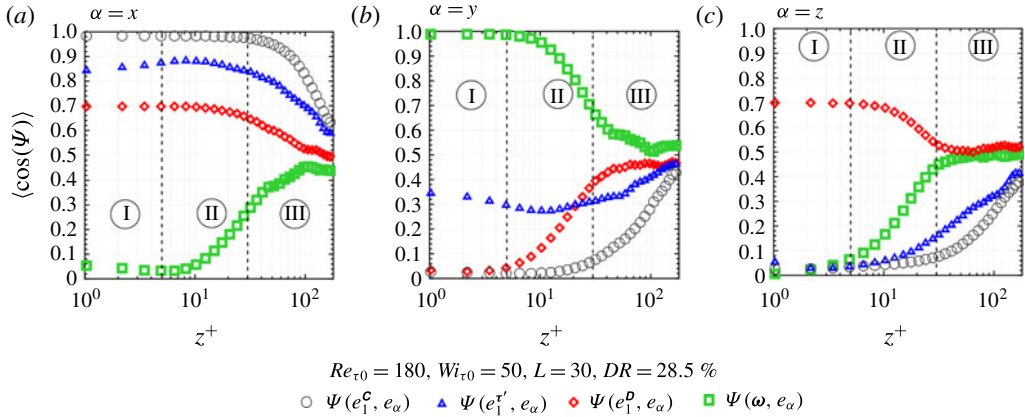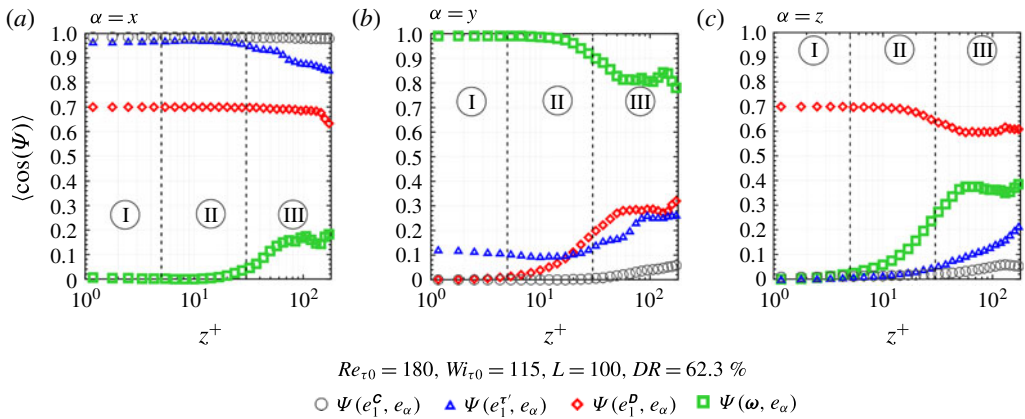
FIGURE 7. (Colour online) Average values in the x–y plane of the cosines of the angles between the principal directions of a given tensor and the three unit vectors e_x, e_y and e_z against the normalized wall distance.

FIGURE 8. (Colour online) Average values in the x–y plane of the cosines of the angles between the principal directions of a given tensor and the three unit vectors e_x, e_y and e_z, against the normalized wall distance.

oriented along the streamwise direction. This preferential alignment between e_1^C and e_x is maintained within the buffer layer. However, it weakens as $\langle \cos \Psi(e_1^C, e_y) \rangle$ and $\langle \cos \Psi(e_1^C, e_z) \rangle$ increase from $z^+ = 30$ to $z^+ = 180$, at which point both profiles reach a peak (≈ 0.4) and $\langle \cos \Psi(e_1^C, e_x) \rangle$ exhibits its minimum value (≈ 0.6). Nevertheless, it is worth noting that even in the LDR middle region, where the Reynolds stresses are more pronounced, a slight preferential orientation of $\boldsymbol{C}$ with e_x is observed. A comparison of figures 7 and 8 reveals that $\cos \Psi(e_1^C, e_x)$ is an increasing function of the elasticity. In the HDR case, the angle between e_1^C and e_x is approximately zero for all z^+, indicating that the polymers are strongly aligned with the streamwise direction throughout the whole channel.

The alignment between the first principal direction of $\boldsymbol{\tau}'$ and e_x for the LDR case displayed in figure 7(a) is accentuated at the wall (≈ 0.85), where $\langle \cos \Psi(e_1^{\tau'}, e_x) \rangle$ is approximately 6 % greater than that of the Newtonian case. In addition, the peak

magnitude of $\langle \cos \Psi (e_1^{\tau'}, e_x) \rangle$, which is located in the buffer layer ($z^+ \approx 8.2$), is also 6 % larger than for the Newtonian flow. As the wall distance increases, the alignment between $e_1^{\tau'}$ and e_x decreases, achieving its minimum value ($\langle \cos \Psi (e_1^{\tau'}, e_x) \rangle \approx 0.6$) at the middle of the channel. Analysing the angles between $e_1^{\tau'}$ and both spanwise and wall-normal directions, we initially note that at the wall, $\langle \cos \Psi (e_1^{\tau'}, e_y) \rangle \approx 0.35$ and $\langle \cos \Psi (e_1^{\tau'}, e_z) \rangle = 0$. The increasing fluctuation in the streamwise velocity in the buffer layer favours the alignment between τ' and e_x, which reduces $\langle \cos \Psi (e_1^{\tau'}, e_y) \rangle$ to its minimum value (≈ 0.3) at $z^+ \approx 15$. After this point, similar to the Newtonian behaviour, $\langle \cos \Psi (e_1^{\tau'}, e_y) \rangle$ and $\langle \cos \Psi (e_1^{\tau'}, e_z) \rangle$ increase, reaching their peak magnitude (≈ 0.45) at the middle of the channel. Since, at this location, $\langle \cos \Psi (e_1^{\tau'}, e_x) \rangle \approx 0.6$, we can conclude that the addition of a polymer reduces the initial random tendency of the orientation of τ' observed for the Newtonian flow. This polymer effect is more clearly perceived in figure 8(*a–c*). In the HDR case, $\langle \cos \Psi (e_1^{\tau'}, e_x) \rangle$ changes from 0.96, at the wall, to the maximum value of 0.98 within the region II. In contrast, $\langle \cos \Psi (e_1^{\tau'}, e_x) \rangle$ decreases across the region III, reaching its minimum value (≈ 0.85) at $z^+ = 180$. Additionally, $\langle \cos \Psi (e_1^{\tau'}, e_y) \rangle$ changes from 0.12, at $z^+ = 0$, to 0.1, in the region II, after which it starts to increase, achieving its peak magnitude (≈ 0.26) at $z+ = 180$. Moreover, $\langle \cos \Psi (e_1^{\tau'}, e_z) \rangle$ smoothly increases from zero to 0.22 across one half of the channel. Lastly, it is important to note that in the HDR case, $\langle \cos \Psi (e_1^{\tau'}, e_x) \rangle > 0.85$ and $\langle \cos \Psi (e_1^{\tau'}, e_z) \rangle < \langle \cos \Psi (e_1^{\tau'}, e_y) \rangle < 0.3$ for all z^+. In other words, the addition of polymers induces a preferable alignment of τ' with the streamwise direction in the whole channel.

The effects of a polymer on the orientation of the rate of strain in the LDR case are indicated by the red open diamonds in figure 7(*a–c*). In the viscous sublayer, a laminar characteristic eigenvector emerges. Consequently, $\langle \cos \Psi (e_1^{D}, e_x) \rangle = \langle \cos \Psi (e_1^{D}, e_z) \rangle \approx \sqrt{2}/2$, and $\langle \cos \Psi (e_1^{D}, e_y) \rangle \approx 0$. These typical orientations gradually change to random orientations at $z^+ = 180$, which differs from the fast transition observed in the Newtonian case, for which a chaotic tendency of alignment is noted throughout the entire log-law region. In the HDR regime, the alignment is not random, as can be seen in figure 8(*a–c*). The angle between e_1^{D} and e_x is equal to 45° from the wall to $z^+ = 155$. In addition, $\langle \cos \Psi (e_1^{D}, e_y) \rangle < 0.5$ and $\langle \cos \Psi (e_1^{D}, e_z) \rangle > 0.4$ for all z^+. Such a behaviour is consistent with the fact that polymers weaken the normal components of $\boldsymbol{D}$ while no significant difference is perceived for its off-diagonal terms compared with the Newtonian case. Thus, polymers act in the flow by partially suppressing the turbulence, making the rate-of-strain tensor more laminar.

Figure 7(*a–c*) also shows the orientation of the vorticity vector in the LDR regime. The green open squares indicate that although the variations of $\langle \cos \Psi (\omega, e_\alpha) \rangle$ across the half-channel are smoother than those for the Newtonian flow, there are similarities between both the LDR and the Newtonian cases, such as the preferable alignment of ω with the y direction in the region I, and the chaotic orientation of this vector within the region III. Nevertheless, the analysis of the alignment of the vorticity for the HDR flow displayed in figure 8(*a–c*) reveals that an increasing elasticity amplifies $\langle \cos \Psi (\omega, e_y) \rangle$, which results from the fact that polymers weaken both $\langle \omega_x \rangle$ and $\langle \omega_z \rangle$ in the region III, but do not affect $\langle \omega_y \rangle$.

Figures 6–8 bring out the complexity of the near-wall dynamics in a Newtonian turbulent flow and how much this region is affected by polymers. In the high drag reduction regime, polymer effects are perceived even far from the wall ($60 < z+ < 180$). The most evident polymer effects shown in these figures are the strong alignment of $\boldsymbol{C}$ and τ' with x, which increase with increasing elasticity.
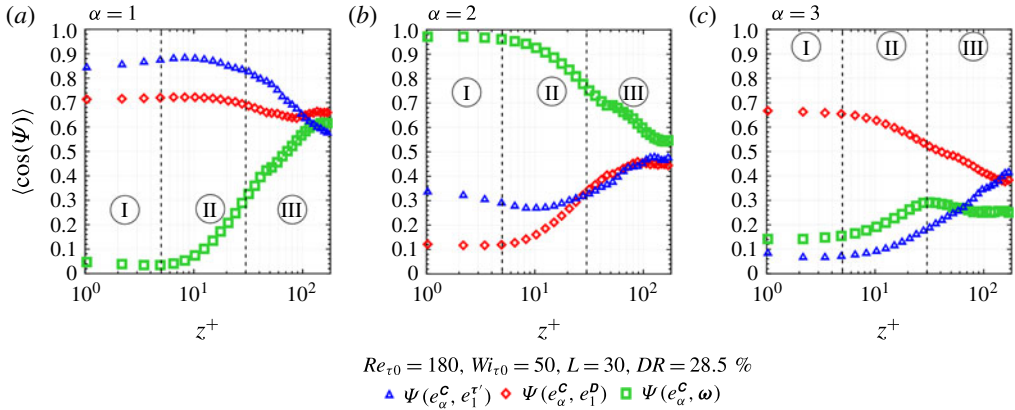
FIGURE 9. (Colour online) Average values in the x–y plane of the cosines of the angles between the principal directions of the conformation tensor and other relevant entities.

These preferable streamwise orientations indicate not only that the most significant turbulence–polymer energy exchanges should occur in the x direction, but also that $\boldsymbol{C}$ and $\boldsymbol{\tau}'$ present an significant alignment between them, which can be linked with the coil–stretch process of the polymer. Thus, in order to clarify the role played by the three considered tensors in the polymer extension mechanism, it is convenient to compute their alignments with respect to the local conformation tensor (the eigenvectors of $\boldsymbol{C}$ are the local reference frames), as shown in figures 9 and 10 for the same LDR and HDR regimes previously analysed in this subsection.

The cosines of the angles between the eigenvectors of $\boldsymbol{C}$ and $e_1^{\tau'}$ in the LDR case are displayed in figure 9. Following the blue open triangles in figure 9(a), we notice that $\langle \cos \Psi(e_1^{\boldsymbol{C}}, e_1^{\tau'}) \rangle$ departs from an accentuated value at the wall (≈ 0.85). Furthermore, the alignment between $e_1^{\boldsymbol{C}}$ and $e_1^{\tau'}$ becomes more pronounced while moving across the viscous sublayer, achieving its peak magnitude (≈ 0.9) at $z^+ = 8.2$, the exact same location as the maximum polymer extension ($\langle \mathrm{tr}(\boldsymbol{C})/L^2 \rangle \approx 0.8$) observed in figure 5. This peak is maintained until $z^+ \approx 12$, from which point $\langle \cos \Psi(e_1^{\boldsymbol{C}}, e_1^{\tau'}) \rangle$ starts to decrease to its minimum value (≈ 0.58), located at the middle of the channel. In contrast, $\langle \cos \Psi(e_2^{\boldsymbol{C}}, e_1^{\tau'}) \rangle$ and $\langle \cos \Psi(e_3^{\boldsymbol{C}}, e_1^{\tau'}) \rangle$ exhibit opposite behaviours across the channel, as shown by the blue open triangles in figure 9(b,c), respectively. The former is small at the wall and, after reaching its minimum value (≈ 0.27) at $z^+ = 8.2$, tends to 0.5. The latter is very close to zero in the viscous sublayer. However, it slightly increases as the wall distance increases, achieving a peak of 0.4 at $z^+ = 180$. In the HDR case, shown in figure 10(a–c), $\langle \cos \Psi(e_1^{\boldsymbol{C}}, e_1^{\tau'}) \rangle$ changes from 0.96, at the wall, to 0.98 at $z^+ \approx 10$, which represents a peak magnitude 9 % greater than that of the LDR case. This value is sustained until $z^+ \approx 15$, from which point the alignment between $e_1^{\boldsymbol{C}}$ and $e_1^{\tau'}$ gently decreases to its minimum value (≈ 0.85), situated at the centre of the channel. In the opposite sense, increasing elasticity decreases $\langle \cos \Psi(e_2^{\boldsymbol{C}}, e_1^{\tau'}) \rangle$ and $\langle \cos \Psi(e_3^{\boldsymbol{C}}, e_1^{\tau'}) \rangle$. It is worth noting that the alignment between the first eigenvectors of $\boldsymbol{C}$ and $\boldsymbol{\tau}'$ is significant even at the middle of the channel, where $\langle \cos \Psi(e_1^{\boldsymbol{C}}, e_1^{\tau'}) \rangle$ is approximately 47 % greater than in the case of the LDR. This indicates that the interaction between $\boldsymbol{C}$ and $\boldsymbol{\tau}'$ is an increasing function of the elasticity, whose effects are perceptible not only near the wall, but also in the region III.
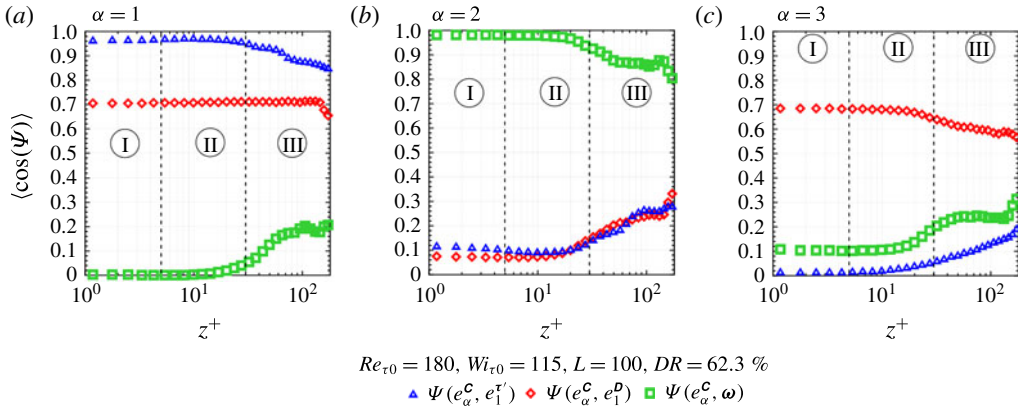
FIGURE 10. (Colour online) Average values in the x–y plane of the cosines of the principal directions of the conformation tensor and other relevant entities.

In the viscous sublayers of both the low and the high drag reduction regimes (figures 9 and 10, respectively), while e_2^C and e_1^D are almost orthogonal, there is an angle of $\approx 45°$ between e_3^C and e_1^D, as well as between e_1^C and e_1^D. Interestingly, $\Psi(e_1^C, e_1^D)$ is maintained across the channel. In contrast, in the LDR scenario, both $\Psi(e_3^C, e_1^D)$ and $\Psi(e_2^C, e_1^D)$ become random as the wall distance increases. However, in the HDR regime, this tendency of chaotic alignment within the region III is attenuated, and, in consequence, $\langle\cos\Psi(e_3^C, e_1^D)\rangle \approx 0.6$ and $\langle\cos\Psi(e_2^C, e_1^D)\rangle \approx 0.25$. Thus, as $Wi_{\tau 0}$ and L increase, the polymer becomes more exposed to the rate-of-strain tensor not only in regions I and II, but also in region III.

Near the wall, the polymer molecules exhibit a weak tendency to lie in the plane perpendicular to $\boldsymbol{\omega}$ since $\langle\cos\Psi(e_1^C, \boldsymbol{\omega})\rangle$ and $\langle\cos\Psi(e_3^C, \boldsymbol{\omega})\rangle$ are almost zero, as can be seen in figures 9 and 10. However, one can note that in this region, $\langle\cos\Psi(e_2^C, \boldsymbol{\omega})\rangle \approx 1.0$. This occurs because, near the wall, e_2^C is oriented along the e_y direction (not shown here), as is $\boldsymbol{\omega}$ (see figures 7 and 8).

5. Polymer–turbulence energy transfer

5.1. *Global exchanges of energy*

As pointed out in previous subsections, near-wall polymers are highly aligned with $\boldsymbol{\tau}'$ and, consequently, strongly exposed to flow stress fluctuations. The latter are responsible for the generation of intermittent quasi-streamwise vortices, which play a very important role in the momentum exchange as well as in the increase of the turbulent friction drag (see Kravchenko, Choi & Moin 1993). Hence, our tensorial and statistical analyses suggest that polymers primarily interact with these intermittent structures, exchanging energy with them. Aiming to characterize such energy exchanges, we consider the work fluctuation terms. These energy terms are that exclusively related to the fluctuating fields which appear in the right-hand side of the work fluctuation equation, which in turn is obtained by decomposing the variables of the momentum equation into mean flow ($\overline{U}_\alpha^+$, $\overline{p}^+$ and $\overline{\Xi}_{\alpha j}^+$) and fluctuations ($u_\alpha'^+$, p'^+ and $\Xi_{\alpha j}'^+$), and then multiplying the resulting equation by the streamwise velocity fluctuations ($u_\alpha'^+$). A detailed deduction of the work equations is provided in appendix A. The work terms exclusively linked with the fluctuating fields are then:
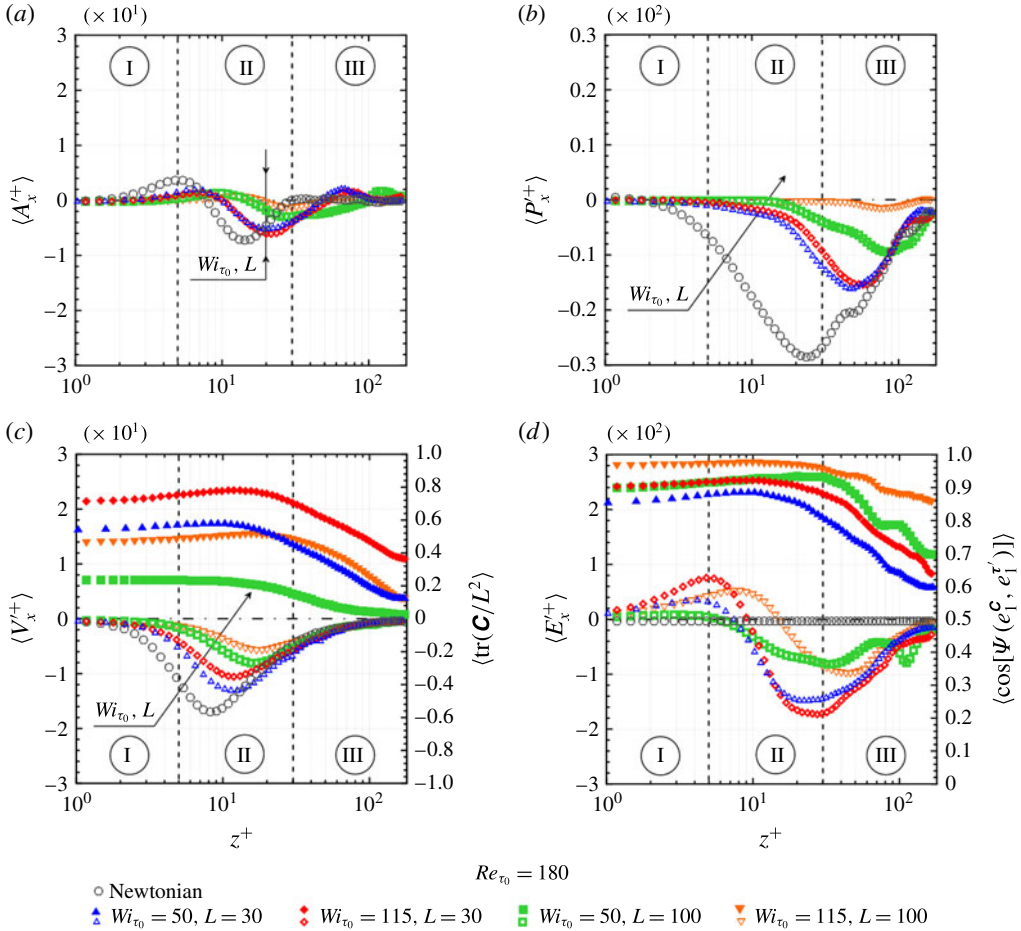
FIGURE 11. (Colour online) The open symbols show the normalized instantaneous streamwise work fluctuating terms against the normalized wall distance. The solid symbols in (c,d) show the profiles of $\langle \text{tr}(\boldsymbol{C})/L^2 \rangle$ and $\langle \cos \Psi(e_1^{\boldsymbol{c}}, e_1^{\tau'}) \rangle$ across the channel half-width, respectively.

$E_\alpha'^+ = (u_\alpha'^+ (\partial \Xi_{\alpha j}'^+ / \partial x_j^+))$, $A_\alpha'^+ = [-u_\alpha'^+ (\partial (u_\alpha'^+ u_j'^+) / \partial x_j^+)]$, $P_\alpha'^+ = (-u_\alpha'^+ (\partial p'^+ / \partial x^+))$ and $V_\alpha'^+ = [(\beta_0) u_\alpha'^+ (\partial^2 u_\alpha'^+ / \partial x_j^{+2})]$. Since the turbulent energy exchanges in the x direction constitute more than 90% of that considering the streamwise, the spanwise and the wall-normal directions, we analyse here only the streamwise work fluctuation terms ($\alpha = x$). Hence, the instantaneous polymer work term, $E_x'^+$, indicates the amount of energy stored ($E_x'^+ < 0$) or released ($E_x'^+ > 0$) by the polymers from the fluctuating velocity field in the streamwise direction, $u_x'^+$ (the fluctuations are denoted by the superscript '$'$'). The supplementary fluctuating work terms denote the advection, $A_x'^+$, the pressure redistribution, $P_x'^+$, and the viscous stress, $V_x'^+$. The sum $A_x'^+ + P_x'^+ + V_x'^+$ is referred to as the Newtonian fluctuating work, $N_x'^+$.

In figures 11 and 12, the x–y plane average of the instantaneous streamwise work fluctuating terms against the normalized wall distance are considered. In addition, both $\langle \text{tr}(\boldsymbol{C})/L^2 \rangle$ and $\langle \cos \Psi(e_1^{\boldsymbol{c}}, e_1^{\tau'}) \rangle$ are plotted. These quantities are denoted by the solid symbols in figures 11(d) and 11(f), respectively. Different levels of elasticity
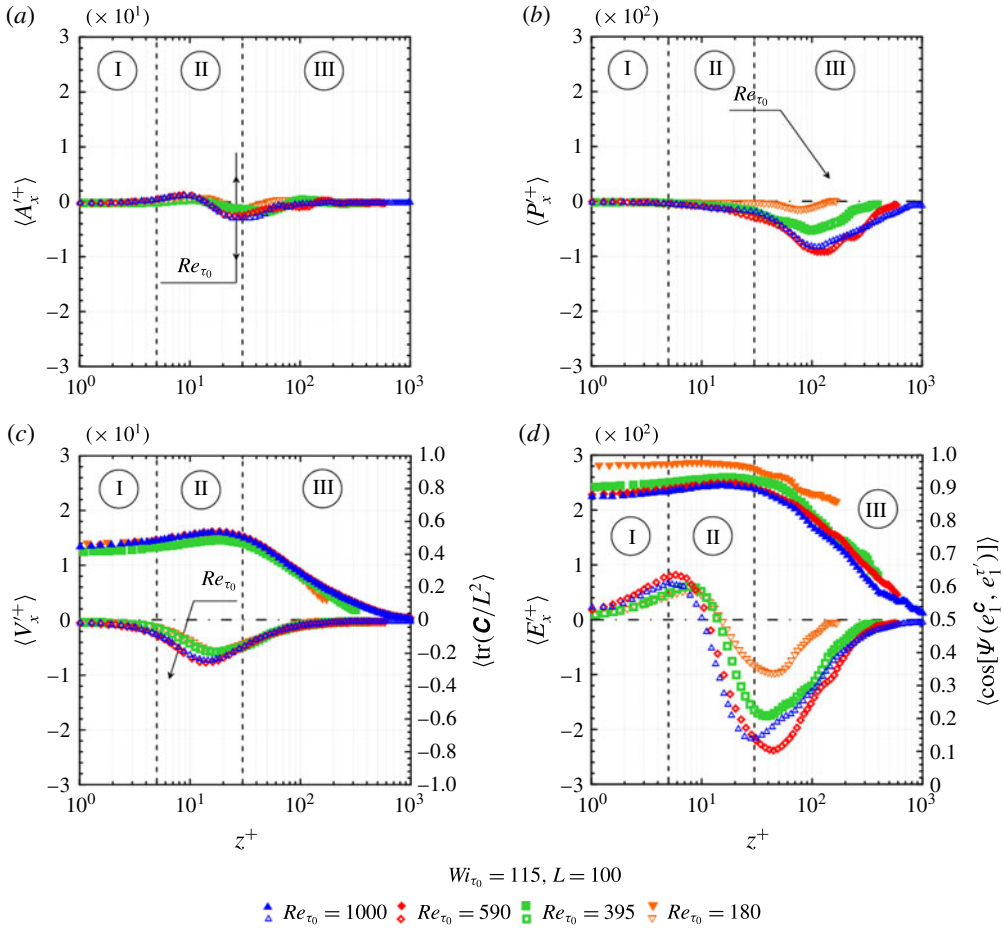
FIGURE 12. (Colour online) The open symbols show the normalized instantaneous streamwise work fluctuating terms against the normalized wall distance. The solid symbols in (*c*,*d*) show the profiles of $\langle \text{tr}(\boldsymbol{C})/L^2 \rangle$ and $\langle \cos \Psi (e_1^{\boldsymbol{c}}, e_1^{\tau'}) \rangle$ across the channel half-width, respectively.

are considered in figure 11 fixing the Reynolds number, while the effects of Re_{τ_0} are shown in figure 12 maintaining $Wi_{\tau_0} = 115$ and $L = 100$. Our lowest Reynolds number case ($Re_{\tau_0} = 180$) and the seven viscoelastic flows detailed in table 1 are considered.

Very close to the wall (I), where the turbulent stresses are negligible, the work fluctuation terms are close to zero. The streamwise viscous work fluctuation (figures 11*c* and 12*c*) and the streamwise polymer work fluctuation (figures 11*d* and 12*d*) exhibit a different behaviour in the vicinity of the wall. For the less elastic case (blue open triangles), the former decreases from the wall to $z^+ \approx 10$, where its minimum value is located. The latter, one order of magnitude smaller than V_x', increases throughout the viscous sublayer, reaching its peak magnitude at $z^+ \approx 5$. It is worth noting that both the inflexion point of $\langle E_x'^+ \rangle$ and the minimum value of $\langle V_x'^+ \rangle$ are located at the same wall distance for each case analysed here. Additionally, the maximum values of $\langle \text{tr}(\boldsymbol{C})/L^2 \rangle$ (solid symbols in figures 11*c* and 12*c*) and $\langle \cos \Psi (e_1^{\boldsymbol{c}}, e_1^{\tau'}) \rangle$ (solid symbols in figures 11*d* and 12*d*), quantities which develop

parallel profiles, are observed at the same location ($z^+ \approx 10$ for the less elastic case). Both the advection and pressure terms become less pronounced as elasticity increases, playing a less important role in the fluctuating energy budget under LDR flow conditions (figure 11). In the opposite trend, more significant values of $\langle A_x'^+\rangle$ and $\langle P_x'^+\rangle$ are observed at higher Re_{τ_0} (figure 12).

The black arrows in figure 11 indicate that increasing elasticity makes $\langle A_x'^+\rangle$, $\langle P_x'^+\rangle$, and $\langle V_x'^+\rangle$ close to zero. This effect of increasing elasticity is more pronounced in the viscous term and, consequently, in the Newtonian term ($A_x'^+ + P_x'^+ + V_x'^+$) of which the minimum value changes from $\langle N_x'^+\rangle \approx 0.225$ for the Newtonian case to $\langle N_x'^+\rangle \approx -0.07$ for the most elastic case (not shown). Furthermore, the minimum and the maximum values observed in figure 11 move away from the wall as Wi_{τ_0} and L increase. On the other hand, as indicated by the black arrows in figure 12, for a fixed elasticity, the magnitude of the energy budget terms increases with increasing Reynolds number.

Intermittent energy transfers may be hidden even by instantaneous spatial-averaging procedures. Further evidence regarding such energy transfers are provided by figure 13, which shows five different joint probability density functions (JPF) for the x–y planes related to the less elastic case and located at $z^+ \approx 5.0$, where $\langle E_z'^+\rangle$ is a maximum, as well as that situated at $z^+ \approx 50$, where $\langle E_z'^+\rangle$ is a minimum (not shown here). The black solid line represents the JPF of E_α' versus u_α' (where α can denote either x or z), whereas the red solid line represents the JPF which considers the instantaneous streamwise polymer work fluctuation and the cosine of the angle between the first principal directions of $\boldsymbol{C}$ and $\boldsymbol{\tau}'$. Similar JPFs are displayed in figure 14 for the Newtonian work fluctuation at the same x–y planes. The work fluctuation terms were normalized by their temporal root mean square spatially averaged over the corresponding x–y plane. In this figure, the most probable events are indicated by internal lines. Although only our less elastic fluid is treated in this figure, all the supplementary viscoelastic cases present qualitatively similar trends.

Firstly, with regard to figure 13(a), it is important to observe that the polymer molecules are allowed to coil ($E_x' > 0$) and stretch ($E_x' < 0$) within the near-wall region ($z^+ \approx 5.0$). At such a location, the polymer molecules are predominantly injecting energy into the flow ($E_x' > 0$) and, as a consequence, increasing both the negative and the positive streamwise velocity fluctuations as well as the absolute value of T_x' (see figure 11). Moreover, this injection of energy is closely related (has a higher probability) to negative values of u_z', as shown in figure 13(b). Interestingly, the red solid lines in figure 13(b) reveal that more pronounced polymer–turbulence exchanges of energy occur when the conformation tensor is predominantly oriented along the first principal direction of $\boldsymbol{\tau}'$ ($\cos \Psi(e_1^{\boldsymbol{C}}, e_1^{\boldsymbol{\tau}'}) \approx 1$), which reinforces the relevance of the alignment between $\boldsymbol{C}$ and $\boldsymbol{\tau}'$ for the polymer–turbulence exchange of energy.

Figure 13 also shows that at $z^+ \approx 50$, polymers primarily extract energy from the flow ($E_z' < 0$), which preferentially occurs where $u_x' < 0$ (figure 13c) and $u_z' < 0$ (figure 13d). However, the suppression of ejection flows ($u_x' < 0$ and $u_z' > 0$; Q2 region) is also a moderately likely event.

Comparing figures 13 and 14, it is interesting to note that in the very near-wall region, E_x' and N_x' tend to have opposite signs. Hence, at $z^+ \approx 5$, injection events are strongly related to $E_x' > 0$ and $N_x' < 0$. Similarly, at $z^+ \approx 50$, the ejection and injection events are linked with $E_z' < 0$ and $N_z' > 0$.

5.2. *Elliptical and hyperbolic exchanges of energy*

In order to better understand the polymer coil–stretch process from the energy perspective, we divide the flow into three different regions by using the Q-criterion discussed in §4.1. Instead of the usual approach, where a threshold is chosen to
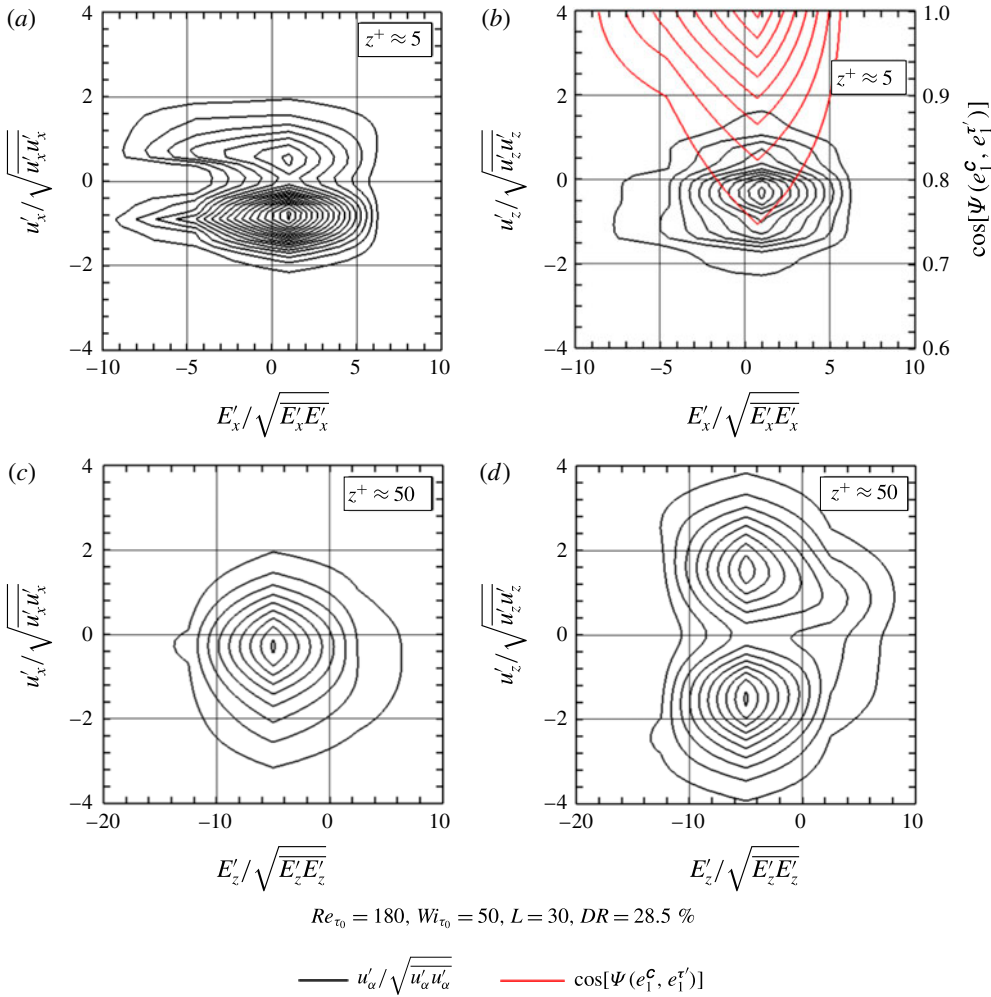
FIGURE 13. (Colour online) Joint probability density functions of instantaneous polymer work versus instantaneous velocity fluctuation for the x–y planes located at $z^+ = 5.0$ (a,b) and $z^+ = 50$ (c,d). Fluctuation terms are normalized by their temporal root mean square spatially averaged over the corresponding x–y plane.

produce a Boolean picture of the flow, as in figure 3, for example, we adopt the Q-criterion as a measure of the intensity of stretching/rotation activity, i.e. we plot the Q field. To this end, Q is normalized in order to produce values between 0 and 1 (Martins *et al.* 2016) and thus takes the form

$$Q_{norm} = \frac{1}{\pi} \cos^{-1} \left(\frac{\|\boldsymbol{W}\|^2 - \|\boldsymbol{D}\|^2}{\|\boldsymbol{W}\|^2 + \|\boldsymbol{D}\|^2} \right). \tag{5.1}$$

Normalized values $0 \leqslant Q_{norm} < 0.5$ represent swirling-like or elliptical regions, whereas $0.5 < Q_{norm} \leqslant 1$ indicates a non-swirling-like or hyperbolic region. A value of $Q_{norm} = 0.5$ represents transition surfaces where the magnitudes of $\boldsymbol{W}$ and $\boldsymbol{D}$ are equal. This normalized vortex identification criterion was applied to the centre x–z plane (at $y = 0.75\pi$) for all viscoelastic flows corresponding to $Re_{\tau_0} = 180$, as shown in figure 15.

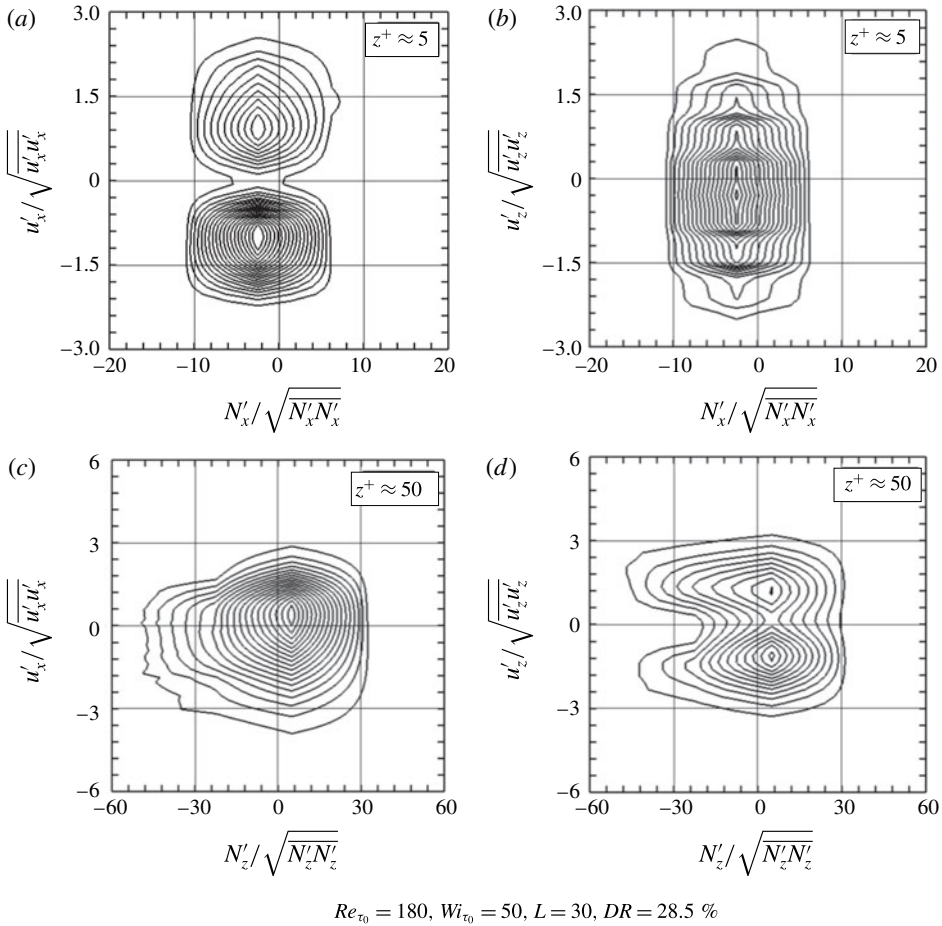$Re_{\tau_0} = 180$, $Wi_{\tau_0} = 50$, $L = 30$, $DR = 28.5 \%$

FIGURE 14. Joint probability density functions of instantaneous Newtonian work versus instantaneous velocity fluctuation over the x–y planes located at $z^+ = 5.0$ (a,b) and $z^+ = 50$ (c,d). Fluctuation terms are normalized by their respective temporal root mean square spatially averaged over the corresponding x–y plane.

The vortical regions (swirling-like) are shown in blue, while the extensional regions (non-swirling-like) are shown in red. Green indicates the transition regions, generally referred to as parabolic, where the intensities of the rotational and extensional motions are close to each other. The lines around vortical regions represent the intersections between the x–y plane and vortices with $Q = 0.01$ (consequently, the lines surround the blue parts). These lines are black or white, which indicates polymer stretching ($E'_x < 0$) or coiling ($E'_x > 0$) in the streamwise direction, respectively.

Analysing figure 15, we first notice that both the vortical and extensional motion are weakened by increasing elasticity. Hence, green regions are more frequent in the HDR cases (c,d). Furthermore, the lines indicate that the morphology of the vortices changes with an increase of Wi_{τ_0} and/or L, since their thicknesses and streamwise lengths increase, while they become more parallel to the wall, something also seen in figure 3. Concerning the polymer–vortex interactions, it is apparent that the lines around the elliptical parts are predominantly black. Such a result reveals that polymers essentially stretch in such a region, extracting energy from the vortices. In addition,
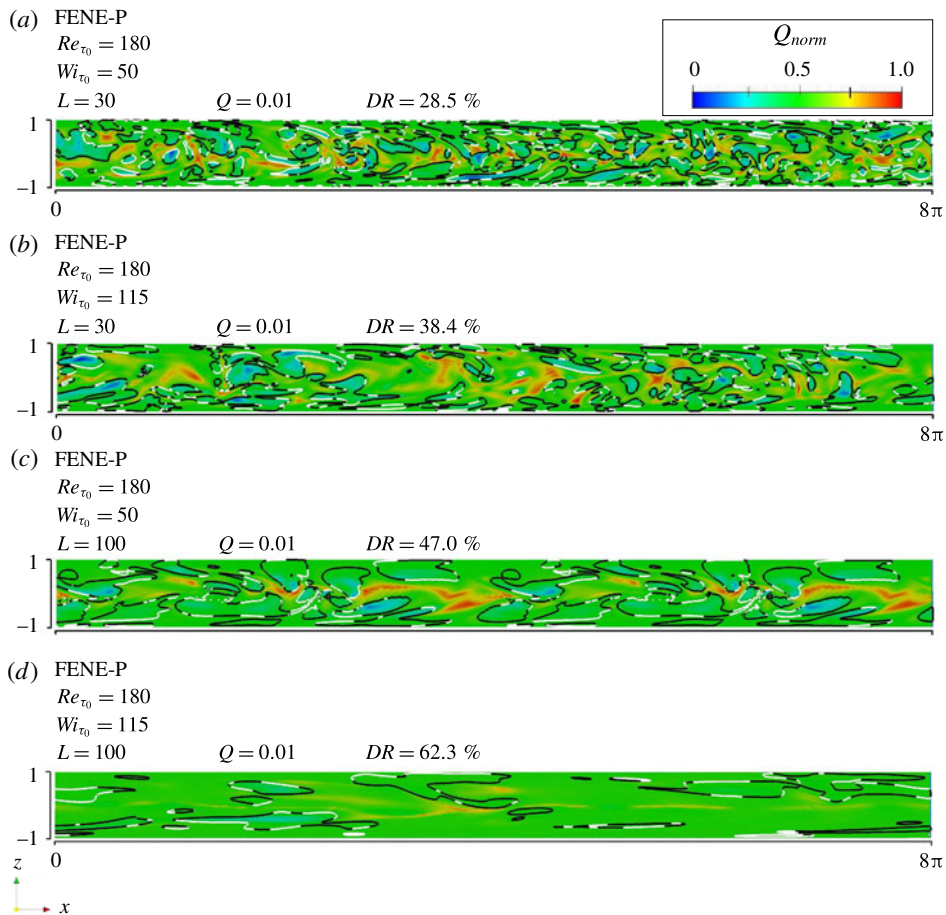
FIGURE 15. (Colour online) Contour of normalized Q-criterion, Q_{norm}. The lines around vortical regions (blue and green regions) represent intersections between the x–y plane and vortices with $Q = 0.01$. These lines are black or white, which indicates polymer stretching or coiling, respectively.

we note that far from the wall, polymers also store a significant amount of energy from the hyperbolic regions, which are mostly surrounded by black lines as well (not shown for clarity).

The extraction of energy from the elliptical and hyperbolic structures by the polymer is further explored in figure 16, where the contours of the normalized Q-criterion were applied to the centre y–z plane (at $x = 4.0\pi$) for our less elastic case. The arrows in figure 16(a) indicate the direction and the sense of the vectors resulting from u'_y and u'_z, while those in figure 16(b) illustrate the direction and the sense of the vectors resulting from polymer force fluctuations ($f'_\alpha = E'_\alpha/u'_\alpha$) in both the spanwise and wall-normal directions (the vector magnitudes are not considered in these figures). Comparing both of these figures, it is apparent that, fundamentally, the polymer forces oppose the vortical motion (blue regions) by imposing a counter-torque around such structures. However, it is important to stress that in the extensional structures (yellow and red regions) the polymer forces also oppose the fluctuating velocities. Similar results were obtained for the other case (not shown here).
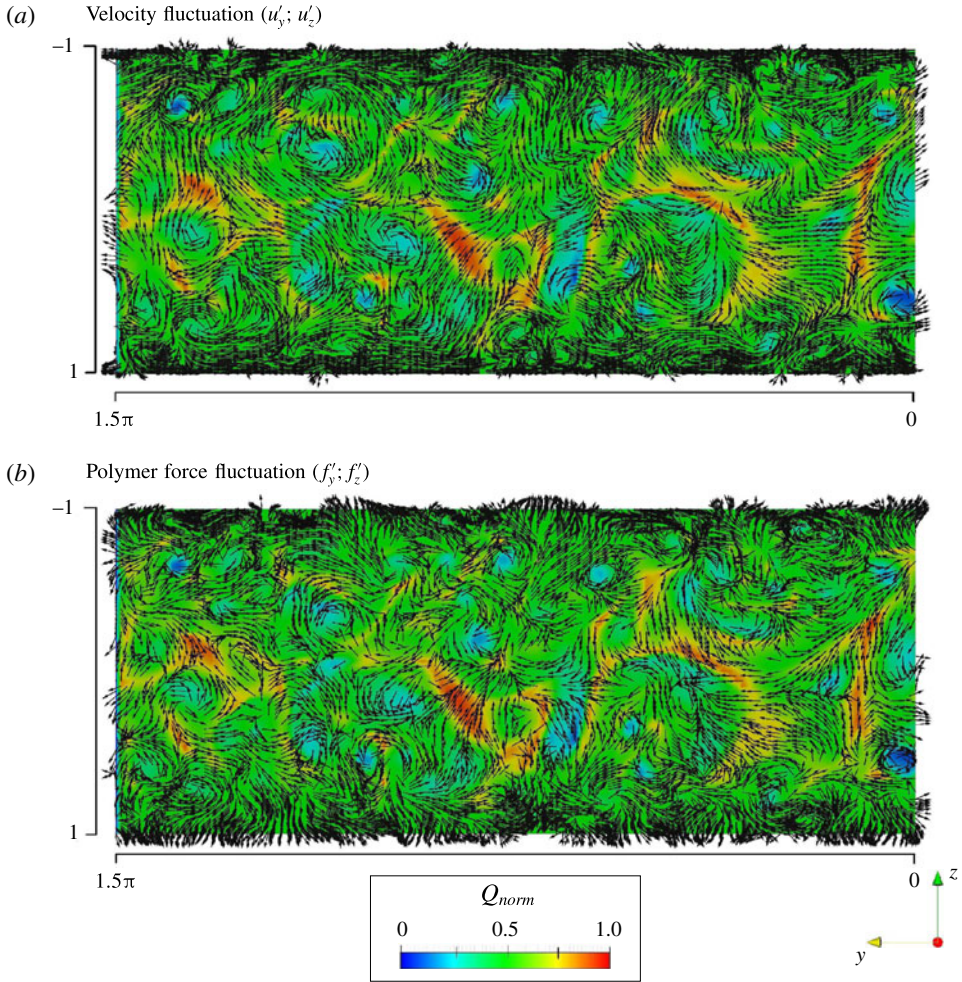
(*a*)   Velocity fluctuation $(u'_y; u'_z)$

(*b*)   Polymer force fluctuation $(f'_y; f'_z)$

FENE-P, $Re_{\tau_0} = 180$, $Wi_{\tau_0} = 50$, $L = 30$, $DR = 28.5\,\%$

FIGURE 16. (Colour online) Velocity (*a*) and polymer body force (*b*) fluctuation vectors on the *y*–*z* plane at $x = 4.0\pi$. Contours of the normalized *Q*-criterion, Q_{norm}, are also overlaid, with blue regions indicating large swirling strength and red regions representing large extensional deformations.

The energy exchanges between the polymers and turbulent structures are highlighted by the open symbols in figures 17 and 18, where the *x*–*y* plane average of the streamwise polymer work fluctuations (*a*) and the streamwise Newtonian work fluctuations (*b*) are plotted against the wall distance for both the elliptical (*c,d*) and the hyperbolic (*e,f*) regions, separately. Additionally, a similar analysis is displayed for $\langle \cos \Psi (e_1^c, e_1^{\tau'}) \rangle$ plotted against z^+ (solid symbols in figures *a,c,e*).

Considering the whole channel evaluated in figures 17(*a,b*) and 18(*a,b*) it is found that polymers essentially release energy within the viscous sublayer, since $\langle E_x'^+(z^+ < 5) \rangle > 0$. In contrast, after reaching its maximum value at $z^+ \approx 5.0$, $\langle E_x'^+ \rangle$ becomes negative and reaches expressive negative values in region II ($20 \leqslant z^+ \leqslant 30$). Negative values of $\langle E_x'^+ \rangle$ are also observed within region III. Hence, the polymers
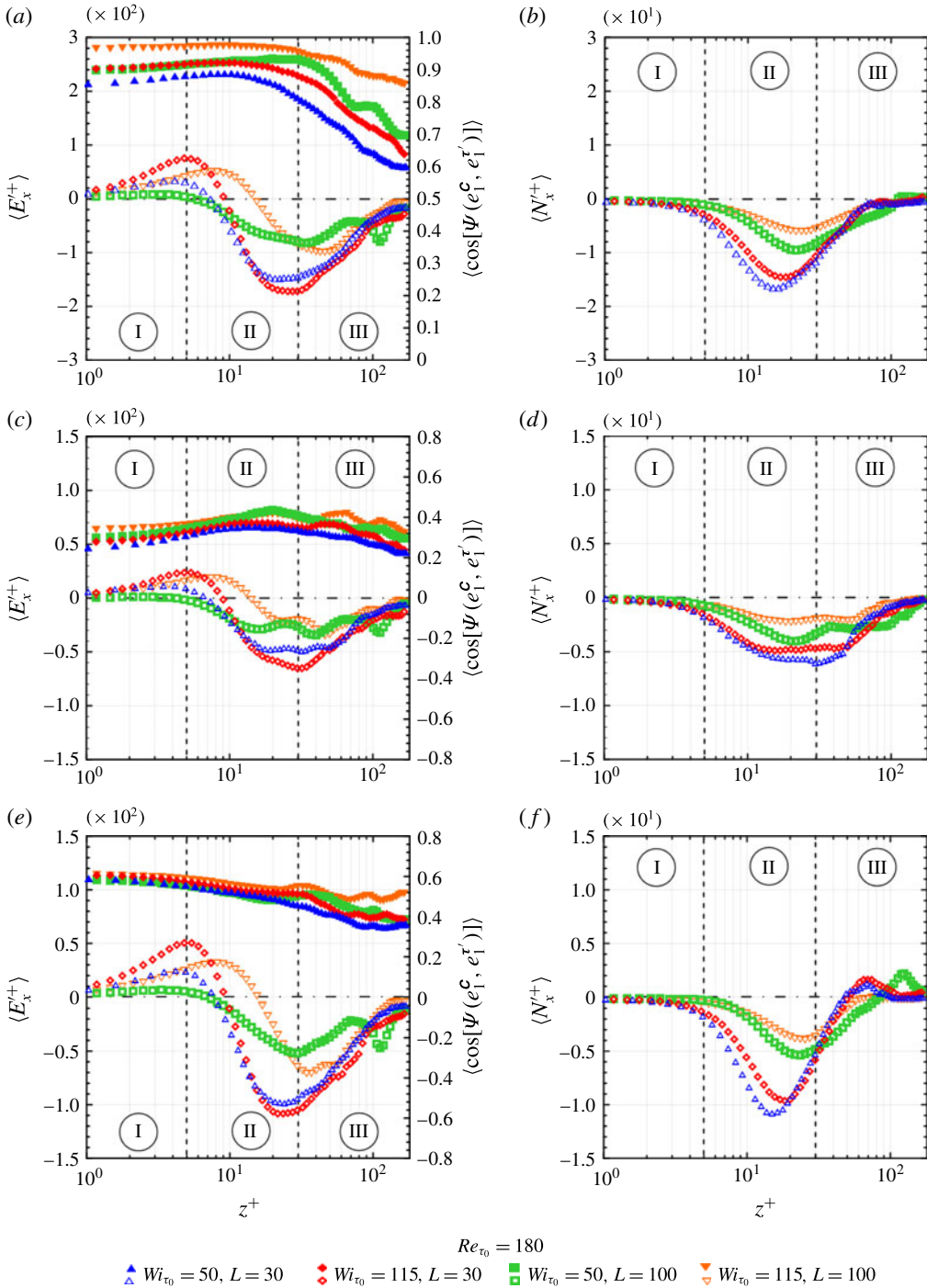
FIGURE 17. (Colour online) The open symbols show the normalized streamwise polymer (*a*,*c*,*e*) and Newtonian (*b*,*d*,*f*) work fluctuations against the wall (z^+) distance considering the whole channel (*a*,*b*) as well as the elliptical (*c*,*d*) and hyperbolic (*e*,*f*) regions, separately. The solid symbols in (*a*,*c*,*e*) show the profile of $\langle \cos \Psi(e_1^{\mathbf{c}}, e_1^{\tau'}) \rangle$ against the wall distance, in the same three domains.
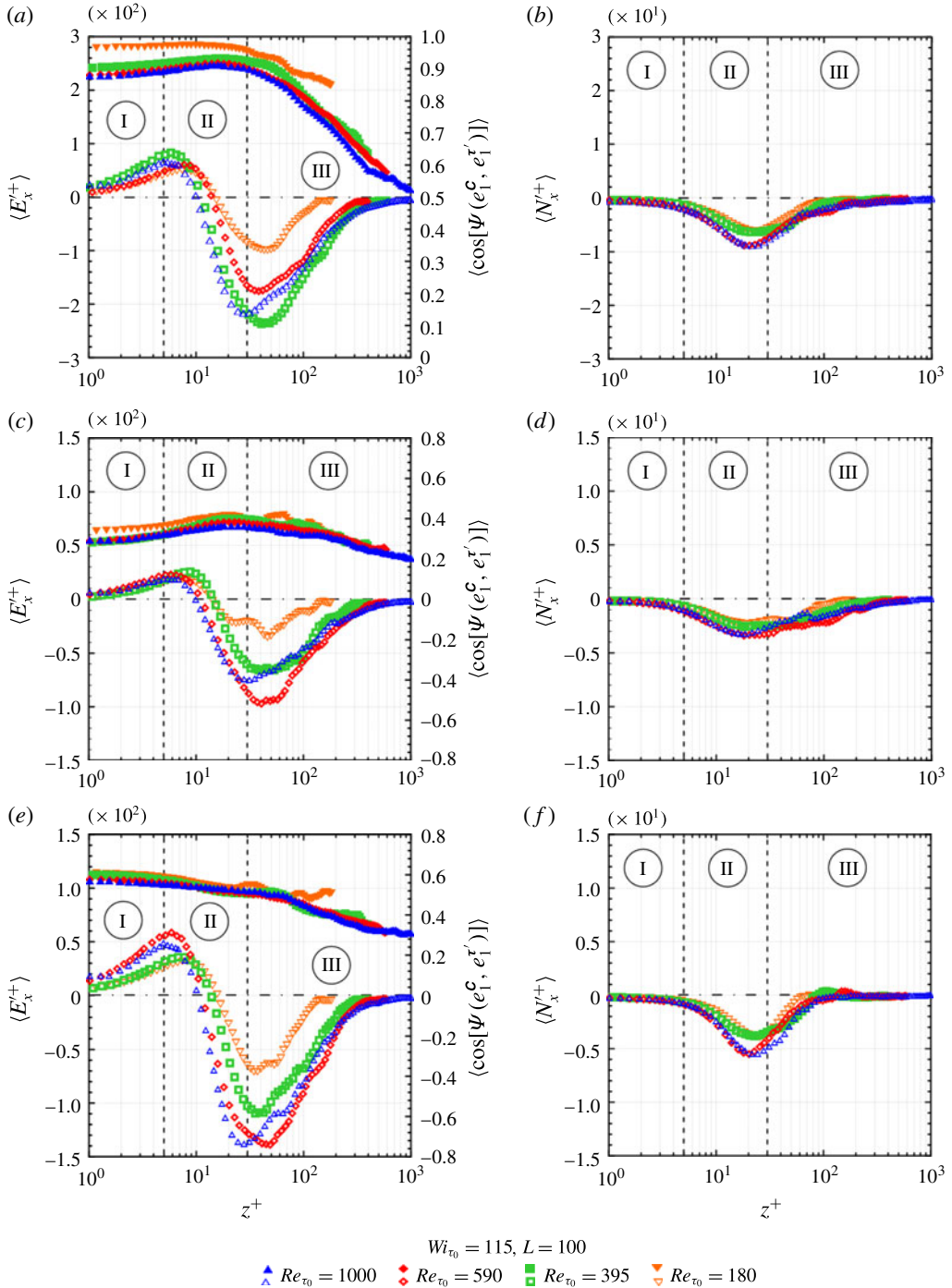
FIGURE 18. (Colour online) The open symbols show the normalized streamwise polymer (a,c,e) and Newtonian (b,d,f) work fluctuations against the wall (z^+) distance considering the whole channel (a,b) as well as the elliptical (c,d) and hyperbolic (e,f) regions, separately. The solid symbols in (a,c,e) show the profile of $\langle \cos \Psi(e_1^c, e_1^{\tau'}) \rangle$ against the wall distance, in the same three domains.

store turbulent energy in both regions II and III ($E'_\alpha < 0$), and release it into the viscous sublayer ($E'_x > 0$) by coiling along the streamwise direction, which increases the streamwise velocity fluctuations (see figure 1b).

Inside the elliptical and hyperbolic structures, the streamwise polymer work fluctuation profiles follow the same trends as those described for the whole channel. Polymers release energy to elliptical (figures 17c and 18c) and hyperbolic (figures 17e and 18e) parts located in the near-wall region (I), which had been previously extracted from such structures in regions II and III. These results corroborate those shown in figure 15. On the other hand, in the wall-normal direction as well as in the spanwise direction (not shown here), the polymer molecules predominantly store turbulent energy from the elliptical and hyperbolic structures by stretching in region III, which reinforces our remarks concerning figure 16. It is important to emphasize that the polymer–turbulence exchanges of energy are more pronounced in hyperbolic regions, especially in the streamwise direction. Lastly, regarding $\langle \cos \Psi(e_1^{\boldsymbol{C}}, e_1^{\tau'}) \rangle$ (solid symbols), the more significant alignments between $\boldsymbol{C}$ and $\boldsymbol{\tau}'$ are situated in the hyperbolic regions (figures 17e and 18e). These alignments decrease monotonically from the viscous sublayer to the centre of the channel.

More significant elastic and inertial effects are observed for $\langle N'^+_x \rangle$ (figures 17b and 18b), which is essentially negative along z^+ and reaches its minimum value in the region II ($z^+ \approx 20$). This term is one order of magnitude greater than $\langle E'^+_x \rangle$ and becomes close to zero as Wi_{τ_0} and L increase, and Re_{τ_0} decreases. Within the elliptical region (figures 17d and 18d), no positive values of $\langle N'^+_x \rangle$ are observed (figures 17d and 18d). However, in the hyperbolic regions (figures 17f and 18f), after achieving its minimum value, $\langle N'^+_x \rangle$ increases and reaches a positive peak magnitude at $z^+ \approx 70$.

Concerning figures 17 and 18, it is also important to note that, for each viscoelastic case, the profiles given by the sum of the energy terms shown in figure 17(c,e), and in figure 18(c,e) at each z^+ are approximately equal to those displayed in figures 17(a) and 18(a), respectively, which is also valid for figures 17(b,d,f) and 18(b,d,f). Such a result indicates that the amount of energy exchanged between the polymers and turbulence in the parabolic regions is negligible compared to that occurring in elliptical or hyperbolic regions.

In order to illustrate the role played by the addition of a polymer in the hyperbolic structures of the domain, consider the hyperbolic counterpart of figure 3. Since the magnitude of the second invariant of the velocity gradient is not altered when one interchanges the Euclidean norms of $\boldsymbol{D}$ and $\boldsymbol{W}$, a negative value of Q with the same magnitude as the ones depicted in figure 3 would give the hyperbolic structure an intensity corresponding to the elliptical structure intensity of that figure, as measured by Q. In this connection, what is seen in figure 19 is a distribution over the domain of hyperbolic structures corresponding to: $Q = -0.7$ for the Newtonian (figure 19a); $Q = -0.7$ for the viscoelastic case with $Wi_{\tau_0} = 50$, $L = 30$ (figure 19b); $Q = -0.7$ for the viscoelastic with $Wi_{\tau_0} = 115$, $L = 30$ (figure 19c); $Q = -0.7$ for the viscoelastic case with $Wi_{\tau_0} = 50$, $L = 100$ (figure 19d); and $Q = -0.1$ for the viscoelastic case with $Wi_{\tau_0} = 115$, $L = 100$ (figure 19e). A direct comparison between figures 3 and 19 shows a remarkable similarity in the intensity of the structures. Although there are clear differences in the morphology of the corresponding hyperbolic structures, figure 19 shows that these turbulent entities are also weakened by the action of the polymer. As the elastic character of the polymer becomes more prominent, the hyperbolic structures are reduced in intensity and size in a quite similar fashion to what happened with the elliptical structures displayed in figure 3. We can deduce that the polymer molecules interact with the turbulence, damping the elliptical and hyperbolic turbulent structures and leading to a tendency of a dominant parabolic character in the flow domain.
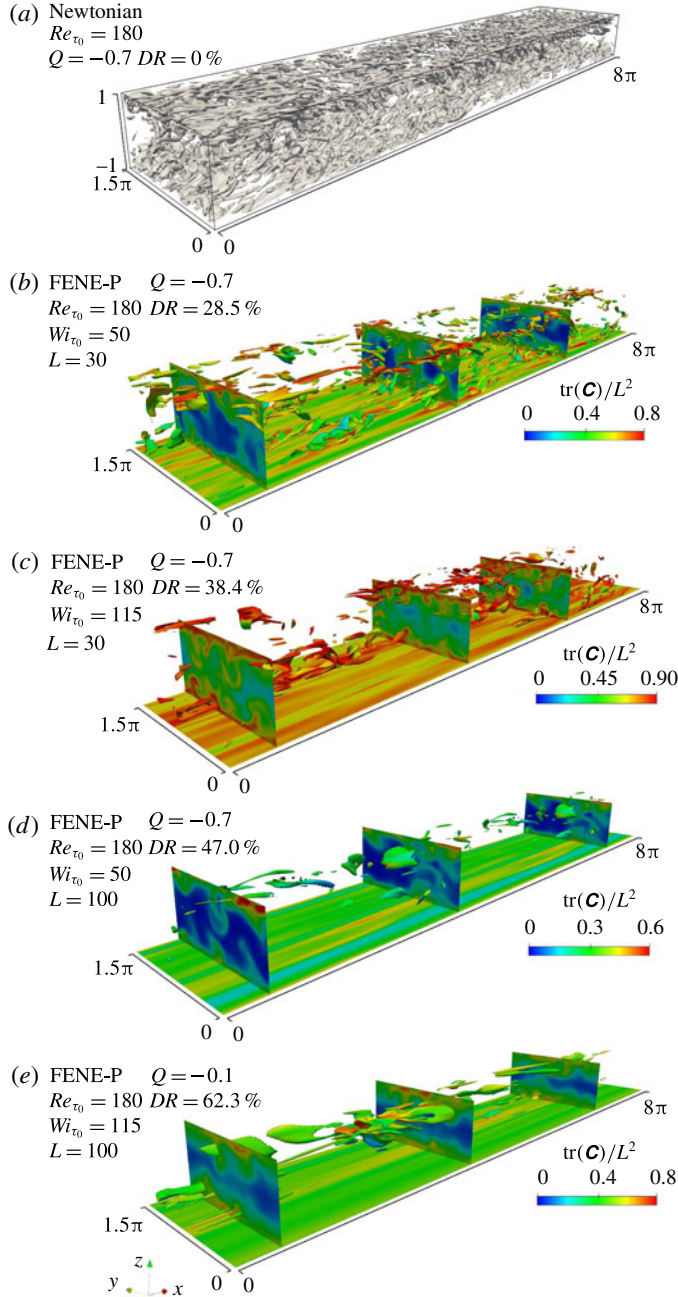
FIGURE 19. (Colour online) The three-dimensional structures represent the isosurfaces of hyperbolic regions defined as a negative value of the second invariant of the velocity gradient tensor, ∇u. The colours indicate polymer stretching, $\mathrm{tr}(\boldsymbol{C})/L^2$.

6. The DR mechanism

Recently, Andrade, Pereira & Soares (2014) experimentally showed that the polymer drag reduction phenomenon undergoes at least three stages over time: A, B and C,
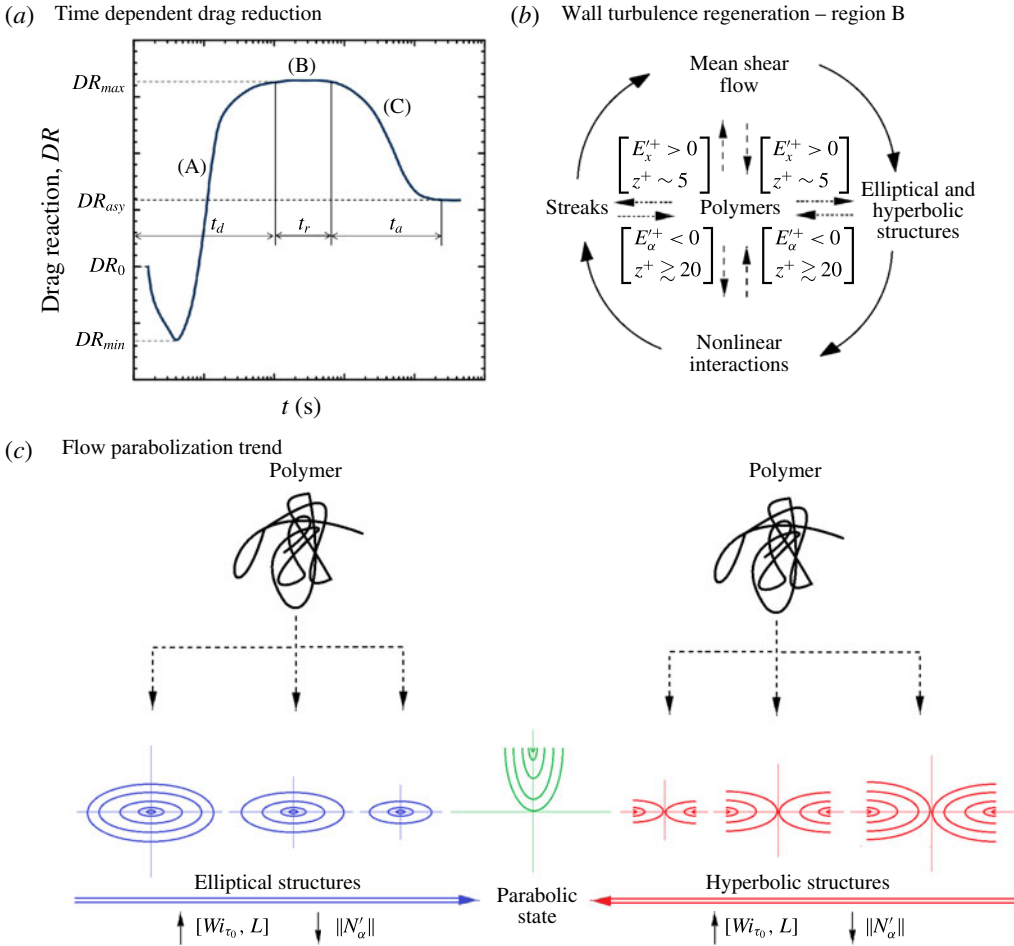
(*a*) Time dependent drag reduction

(*b*) Wall turbulence regeneration – region B

(*c*) Flow parabolization trend

FIGURE 20. (Colour online) Sketch of the polymer-induced drag reduction mechanism.

as shown in figure 20(*a*). In stage A, referred to as the developing time (t_d), the DR is first negative, due to an instantaneous increase in the local extensional viscosity caused by a large and abrupt polymer stretching. This initial process requires a significant energy input, which comes predominantly from the mean flow (Pereira *et al.* 2017), besides a lesser but still important amount of energy that is extracted from the elliptical and hyperbolic structures, since the polymers are strongly exposed to $\boldsymbol{\tau}'$. After reaching a minimum value (DR_{min}), the polymers start their coil–stretch cycle and, in consequence, the DR increases in response to the polymer-flow interactions, achieving a maximum value (DR_{max}), which makes for the beginning of stage B. The duration of stage B is referred to as the resistance time (t_r). Such a stage is characterized by a negligible polymer degradation, during which the DR is maintained at its maximum value. In order to describe the polymer coil–stretch mechanisms during stage B, we invoke the autonomous regeneration cycle discussed by Dubief *et al.* (2004), in which we include new details concerning the polymer–turbulent exchanges of energy shown in figure 20(*b*). This autonomous cycle is originally based on that put forward by Jiménez & Pinelli (1999) and conceived for Newtonian turbulent flows. In the viscous sublayer, the polymers are

highly exposed to the mean flow, which acts as a source of elastic potential energy (see Thais *et al.* 2013). Additionally, just above the viscous sublayer ($z^+ \approx 5$), the polymers enhance the streamwise momentum in the elliptical and hyperbolic regions by releasing streamwise turbulent energy ($E'_x > 0$) to such structures (see figure 17). However, polymers can be also pulled around the near-wall vortices, passing through hyperbolic regions and experiencing a significant strain within both these turbulent structures. Thereby, as shown in figure 17, the polymers store turbulent energy from the elliptical and hyperbolic parts ($E'_\alpha < 0$) in regions II and III (where they probably also release a non-negligible amount of energy to the mean flow). Lastly, the polymer can be injected (or re-injected) into the very near-wall region, there releasing streamwise turbulent energy and being more exposed to the mean shear. It is worth mentioning that, as shown by the red JPF in figure 13(*b*), more pronounced polymer–turbulence exchanges of energy occur where $\cos \Psi(e_1^C, e_1^{\tau'}) \approx 1$.

Since the amount of energy stored by the polymer from the fluctuating velocity field in regions II and III is greater than that released just above the viscous sublayer, there is a weakening of the elliptical and hyperbolic turbulent structures, as indicated by both the blue and red arrows in figure 20(*c*), resulting in the growth of the parabolic domain. This flow parabolization trend is accompanied by the reduction of the Newtonian work fluctuation as the elasticity increases.

During their coil–stretch cycle, polymer molecules can be mechanically degraded as a result of excessive polymer stretching, which reduces their ability to act as energy exchange agents. Hence, when polymer degradation becomes pronounced, the DR decreases, as represented by stage C in figure 20(*a*), until achieving an asymptotic value (DR_{asy}), which indicates that the degradation has stopped and the molecular weight distribution has reached a steady state.

The coil–stretch mechanism discussed above and sketched in figure 20 highlights the role played by the polymers in the self-sustained wall turbulence interacting with the mean shear, nonlinear interactions, near-wall elliptical and hyperbolic structures in viscoelastic drag reducing flows, considering a DR which evolves over time from the very start of the phenomenon until reaching its asymptotic value.

7. Concluding remarks

The statistical and tensorial analysis of the polymer coil–stretch mechanism in a drag reducing channel flow were conducted by using direct numerical simulations employing the viscoelastic FENE-P model. Four Newtonian flow and seven viscoelastic flows were examined, keeping the viscosity ratio β_0 fixed at 0.9 and taking into account four different values of the zero shear friction Reynolds number ($Re_{\tau_0} = 180$, $Re_{\tau_0} = 395$, $Re_{\tau_0} = 590$ and $Re_{\tau_0} = 1000$) and two different values of the friction Weissenberg number and the maximum polymer molecule extensibility ($Wi_{\tau_0} = 50$; $Wi_{\tau_0} = 115$; $L = 30$; $L = 100$), which provided drag reduction regimes from 28.5 % up to 62.3 % (the simulation details are in table 1, § 2).

The polymer modifies the mean flow velocity, increasing its streamwise component, which departs from the Prandtl–Kármán law (the onset of DR) up to Virk's asymptote, as Wi_{τ_0} and L increase. A similar effect is found for the streamwise Reynolds stress normal component, although the other normal components of this tensor decrease (figure 1 in § 3). Concerning the relative polymer extension, the polymer molecules exhibit a significant stretch level close to the wall, which reaches its maximum within the buffer layer but is minimal, yet still relevant, at the centre of the channel. Such an extension profile cannot, however, be sustained exclusively by the mean flow,

although the mean viscous shear stress is the most relevant stretch agent in the very near-wall region (figure 2 in §3). As pointed out in §4, the stretching produced by the mean flow is increased, since the turbulent structures interact with the polymers molecules, providing a supplementary polymer extension. In fact, polymer molecules are strongly exposed to flow stress fluctuations, which is evidenced by the high degree of alignment between the instantaneous conformation tensor and the instantaneous velocity fluctuation product tensor (especially in the very near-wall region). As Wi_{τ_0} and L increase, this alignment between both the first principal directions of the conformation tensor ($\boldsymbol{C}$) and the velocity fluctuation product tensor ($\boldsymbol{\tau}'$) becomes more pronounced.

The thickening of the buffer layer was also evidenced by the tensorial and statistical analysis, as shown in §4.2. For the most viscoelastic flow, for instance, the angle between $e_1^{\boldsymbol{D}}$ and e_x is equal to 45° from the wall to $z^+ = 155$, a typical orientation which indicates that the polymers act on the flow by partially suppressing the turbulence, making the rate-of-strain tensor more laminar, viscometrically speaking.

The Q-criterion was used as a measure of the intensity of elliptical (vortices) and hyperbolic structures. A normalized dimensionless version of this criterion was constructed in order to partition the domain into elliptical, hyperbolic and parabolic regions. The strong interactions between the polymers and intermittent turbulent structures were investigated using perspective of the Q-criterion (§5). Figure 16 showed that the previously documented counter-torque action (see Kim *et al.* 2007, 2008) on the turbulent elliptical structures (vortices) corresponding to blue regions where $Q_{norm} < 0.5$ (or $Q > 0$) is accompanied by a counter-stretch force acting on the hyperbolic structures corresponding to red regions where $Q_{norm} > 0.5$ (or $Q < 0$). To illustrate the polymer–turbulence interactions in the hyperbolic structures, figure 19 showed how these structures are weakened as the elasticity is increased from the Newtonian to our maximum drag reduction case. The similarities with respect to the effect on the elliptical structures in terms of the intensity of the structures are remarkable (see figure 3). The conclusion reached at this point was schematically represented in figure 20(*c*). An important consequence of the addition of a polymer to turbulent shear flows is the weakening of elliptical and hyperbolic structures, inducing the enhancement of the parabolic domain, which is typical of a viscometric laminar response to an imposed shear flow.

The instantaneous turbulent energy exchange represented by the streamwise work fluctuation terms (§5) was analysed in this paper by splitting the domain into elliptical and hyperbolic flow regions. Such analyses, combined with the tensorial and statistical ones, allowed us to include more details concerning the polymer coil–stretch mechanism on the autonomous regeneration cycle discussed by Dubief *et al.* (2004) and originally based on that put forward by Jiménez & Pinelli (1999) conceived for Newtonian turbulent flows. The Newtonian fluctuating term, $\langle N_x'^+ \rangle$ exceeds by one order of magnitude the elastic fluctuating term, $\langle E_x'^+ \rangle$, revealing an important manifestation of the nonlinearity of the problem, and, therefore, needs to be taken into account in the description of the DR mechanism. We have noticed higher intensities of these quantities in the hyperbolic domain than in the elliptical ones. In the very near-wall region, polymers not only release energy to the streaks (as previously pointed out by Dubief *et al.* 2004; Terrapon *et al.* 2004), but also to the elliptical and hyperbolic structures. However, these two turbulent structures are damped within the buffer layer. Joint probability functions have shown that more pronounced polymer–turbulence exchanges of energy occur when the conformation tensor is predominantly oriented along the first principal direction of $\boldsymbol{\tau}'$ (figure 13).

Fundamentally, in elliptical regions, the polymer stores turbulent energy by applying a counter-torque around the vortices, damping the ejection (Q2) and sweep (Q4) events, while, in the hyperbolic regions, polymers take energy from the flow by opposing the extensional deformation. Lastly, it is important to remark that a polymer release of energy occurs almost exclusively in the streamwise direction since $\langle E_y'^+ \rangle \leqslant 0$ and $\langle E_z'^+ \rangle \leqslant 0$ across the channel half-width (not shown here), which is in agreement with the increase in the velocity streamwise fluctuation observed in drag reducing flows. Polymers store energy from the mean flow (as recently reported by Thais *et al.* 2013) in order to have a considerable stretch in the very near-wall region, and we believe that they can also release energy to the mean flow within the buffer layer, a fact with which the increase in u_x' could be also related, since the mean flow also acts as a source of turbulent kinetic energy in this region.

Acknowledgements

Appendix A

In this work, we are focusing our analysis on the energy terms exclusively related with the fluctuating fields. As shown in §4, our tensorial and statistical analyses indicate that the conformation tensor is considerably exposed to the Reynolds stress tensor, which suggests a strong energy transfer between the polymers and the turbulent structures. Aiming to characterize such energy exchanges, we consider the work fluctuating terms. These energy terms are those exclusively related to the fluctuating fields which appear in the right-hand side of the work equations, which in turn are obtained by decomposing the variables of the momentum equations into mean components ($\overline{U}_\alpha$, $\overline{p}$ and $\overline{\Xi}_{\alpha j}$) and fluctuation ones ($u_\alpha'$, p' and $\Xi_{\alpha j}'$), and then multiplying the resulting equations by the velocity fluctuation (u_α').

We provide below a deduction of the work equations considering, initially, the scaled momentum equations:

$$\frac{\partial u_\alpha}{\partial t} + u_j \frac{\partial u_\alpha}{\partial x_j} = -\frac{\partial p}{\partial x_\alpha} + \frac{\beta_0}{Re_h}\frac{\partial^2 u_\alpha}{\partial x_j^2} + \frac{1}{Re_h}\frac{\partial \Xi_{\alpha j}}{\partial x_j}. \quad (A\,1)$$

The variables of the momentum equations are then decomposed into mean components ($\overline{U}_\alpha$, $\overline{p}$ and $\overline{\Xi}_{\alpha j}$) and fluctuating ones ($u_\alpha'$, p' and $\Xi_{\alpha j}'$):

$$\frac{\partial(\overline{U}_\alpha + u_\alpha')}{\partial t} + (\overline{U}_j + u_j')\frac{\partial(\overline{U}_\alpha + u_\alpha')}{\partial x_j}$$
$$= -\frac{\partial(\overline{p} + p')}{\partial x_\alpha} + \frac{\beta_0}{Re_h}\frac{\partial^2(\overline{U}_\alpha + u_\alpha')}{\partial x_j^2} + \frac{1}{Re_h}\frac{\partial(\overline{\Xi}_{\alpha j} + \Xi_{\alpha j}')}{\partial x_j}. \quad (A\,2)$$

Then,

$$\frac{\partial(\overline{U}_\alpha)}{\partial t} + \frac{\partial(u'_\alpha)}{\partial t} + (\overline{U}_j)\frac{\partial(\overline{U}_\alpha)}{\partial x_j} + (\overline{U}_j)\frac{\partial(u'_\alpha)}{\partial x_j} + (u'_j)\frac{\partial(\overline{U}_\alpha)}{\partial x_j} + (u'_j)\frac{\partial(u'_\alpha)}{\partial x_j}$$
$$= -\frac{\partial(\overline{p})}{\partial x_\alpha} - \frac{\partial(p')}{\partial x_\alpha} + \frac{\beta_0}{Re_h}\frac{\partial^2(\overline{U}_\alpha)}{\partial x_j^2} + \frac{\beta_0}{Re_h}\frac{\partial^2(u'_\alpha)}{\partial x_j^2} + \frac{1}{Re_h}\frac{\partial(\overline{\Xi}_{\alpha j})}{\partial x_j} + \frac{1}{Re_h}\frac{\partial(\Xi'_{\alpha j})}{\partial x_j}. \quad \text{(A 3)}$$

Rearranging the terms,

$$\frac{\partial(\overline{U}_\alpha)}{\partial t} + \frac{\partial(u'_\alpha)}{\partial t} = \left[-\overline{U}_j\frac{\partial\overline{U}_\alpha}{\partial x_j}\right] + \left[-\frac{\partial\overline{p}}{\partial x_\alpha}\right] + \left[\frac{\beta_0}{Re_h}\frac{\partial^2\overline{U}_\alpha}{\partial x_j^2}\right] + \left[\frac{1}{Re_h}\frac{\partial\overline{\Xi}_{\alpha j}}{\partial x_j}\right]$$
$$+ \left[-\overline{U}_j\frac{\partial u'_\alpha}{\partial x_j}\right] + \left[-u'_j\frac{\partial\overline{U}_\alpha}{\partial x_j}\right]$$
$$+ \left[-u'_j\frac{\partial u'_\alpha}{\partial x_j}\right] + \left[-\frac{\partial p'}{\partial x_\alpha}\right] + \left[\frac{\beta_0}{Re_h}\frac{\partial^2 u'_\alpha}{\partial x_j^2}\right] + \left[\frac{1}{Re_h}\frac{\partial\Xi'_{\alpha j}}{\partial x_j}\right]. \quad \text{(A 4)}$$

Multiplying the resulting equations by the velocity fluctuations (u'_α):

$$u'_\alpha\frac{\partial(\overline{U}_\alpha)}{\partial t} + u'_\alpha\frac{\partial(u'_\alpha)}{\partial t}$$
$$= \left[-u'_\alpha\overline{U}_j\frac{\partial\overline{U}_\alpha}{\partial x_j}\right] + \left[-u'_\alpha\frac{\partial\overline{p}}{\partial x_\alpha}\right] + \left[u'_\alpha\frac{\beta_0}{Re_h}\frac{\partial^2\overline{U}_\alpha}{\partial x_j^2}\right] + \left[u'_\alpha\frac{1}{Re_h}\frac{\partial\overline{\Xi}_{\alpha j}}{\partial x_j}\right]$$
$$+ \left[-u'_\alpha\overline{U}_j\frac{\partial u'_\alpha}{\partial x_j}\right] + \left[-u'_\alpha u'_j\frac{\partial\overline{U}_\alpha}{\partial x_j}\right]$$
$$+ \left[-u'_\alpha u'_j\frac{\partial u'_\alpha}{\partial x_j}\right] + \left[-u'_\alpha\frac{\partial p'}{\partial x_\alpha}\right] + \left[u'_\alpha\frac{\beta_0}{Re_h}\frac{\partial^2 u'_\alpha}{\partial x_j^2}\right] + \left[u'_\alpha\frac{1}{Re_h}\frac{\partial\Xi'_{\alpha j}}{\partial x_j}\right]. \quad \text{(A 5)}$$

Lastly, since the flow is incompressible ($\nabla \cdot u = 0$), we can rewrite the advection terms as $[-u'_\alpha\overline{U}_j(\partial\overline{U}_\alpha/\partial x_j)] = [-u'_\alpha(\partial(\overline{U}_\alpha\overline{U}_j)/\partial x_j)]$, $[-u'_\alpha\overline{U}_j(\partial u'_\alpha/\partial x_j)] = [-u'_\alpha(\partial(u'_\alpha\overline{U}_j)/\partial x_j)]$, $[-u'_\alpha u'_j(\partial\overline{U}_\alpha/\partial x_j)] = [-u'_\alpha(\partial(\overline{U}_\alpha u'_j)/\partial x_j)]$, and $[-u'_\alpha u'_j(\partial u'_\alpha/\partial x_j)] = [-u'_\alpha(\partial(u'_\alpha u'_j)/\partial x_j)]$. Hence, the work equations assume the following form:

$$\left[u'_\alpha\frac{\partial(\overline{U}_\alpha)}{\partial t}\right] + \left[\frac{1}{2}\frac{\partial(u'^2_\alpha)}{\partial t}\right]$$
$$= \left[-u'_\alpha\frac{\partial(\overline{U}_\alpha\overline{U}_j)}{\partial x_j}\right] + \left[-u'_\alpha\frac{\partial\overline{p}}{\partial x_\alpha}\right] + \left[\frac{\beta_0}{Re_h}u'_\alpha\frac{\partial^2\overline{U}_\alpha}{\partial x_j^2}\right] + \left[\frac{1}{Re_h}u'_\alpha\frac{\partial\overline{\Xi}_{\alpha j}}{\partial x_j}\right]$$
$$+ \left[-u'_\alpha\frac{\partial(u'_\alpha\overline{U}_j)}{\partial x_j}\right] + \left[-u'_\alpha\frac{\partial(\overline{U}_\alpha u'_j)}{\partial x_j}\right]$$
$$+ \underbrace{\left[-u'_\alpha\frac{\partial(u'_\alpha u'_j)}{\partial x_j}\right]}_{A'_\alpha} + \underbrace{\left[-u'_\alpha\frac{\partial p'}{\partial x_\alpha}\right]}_{P'_\alpha} + \underbrace{\left[\frac{\beta_0}{Re_h}u'_\alpha\frac{\partial^2 u'_\alpha}{\partial x_j^2}\right]}_{V'_\alpha} + \underbrace{\left[\frac{1}{Re_h}u'_\alpha\frac{\partial\Xi'_{\alpha j}}{\partial x_j}\right]}_{E'_\alpha}. \quad \text{(A 6)}$$

In order to evaluate the contribution of each work term as a function of its direction, the summation is not applied to the subscript α ($\alpha = x$ or $\alpha = y$ or $\alpha = z$).

The work terms exclusively linked with the fluctuating fields in the right-hand side of the work equations are then: $A'_\alpha = [-u'_\alpha(\partial(u'_\alpha u'_j)/\partial x_j)]$, $P'_\alpha = (-u'_\alpha(\partial p'/\partial x))$, $V'_\alpha = [(\beta_0/Re_h)u'_\alpha(\partial^2 u'_\alpha/\partial x_j^2)]$ and $E'_\alpha = 1/Re_h(u'_\alpha(\partial \Xi'_{\alpha j}/\partial x_j))$. Since the turbulent energy exchanges in the x direction constitute more than 90% of those exchanges, we analyse only the streamwise work fluctuation terms ($\alpha = x$). Hence, the instantaneous polymer work term, E'_x, indicates the amount of energy stored ($E'_x < 0$) or released ($E'_x > 0$) by the polymers from the fluctuating velocity field in the streamwise direction, u'_x (the fluctuations are denoted by the superscript '′'). The supplementary fluctuating work terms denote the advection, A'_x, the pressure redistribution, P'_x and the viscous stress, V'_x. The sum $A'_x + P'_x + V'_x$ is referred to as the Newtonian fluctuating work, N'_x.

REFERENCES

ADRIAN, R. J. 2007 Hairpin vortex organization in wall turbulence. *Phys. Fluids* **19**, 041301.

ANDRADE, R. M., PEREIRA, A. S. & SOARES, E. J. 2014 Drag increase at the very start of drag reducing flows in a rotating cylindrical double gap device. *J. Non-Newtonian Fluid Mech.* **212**, 73–79.

ARMFIELD, S. W. & STREET, R. L. 2000 Fractional step methods for the Navier–Stokes equations on non-staggered grids. *ANZIAM J.* **42(E)**, C134–C156.

BAGHERI, F., MITRA, D., PERLEKAR, P. & BRANDT, L. 2012 Statistics of polymer extensions in turbulent channel flow. *Phys. Rev. E* **86**, 056314.

BENZI, R., ANGELIS, E. D., L'VOV, V. S. & PROCACCIA, I. 2005 Identification and calculation of the universal asymptote for drag reduction by polymers in wall-bounded turbulence. *Phys. Rev. Lett.* **95**, 194502.

BEWERSDORFF, H. W. 1982 Effect of a centrally injected polymer thread on drag in pipe flow. *Rheol. Acta* **21**, 587–589.

BEWERSDORFF, H. W. & SINGH, R. P. 1988 Rheological and drag reduction characteristics of xanthan gum solutions. *Rheol. Acta* **27**, 617–627.

BIRD, R., ARMSTRONG, R. & HASSAGER, O. 1987 *Dynamics of Polymeric Liquids. Kinetic Theory*. Wiley.

BURGER, E. D. & CHORN, L. G. 1980 Studies of drag reduction conducted over a broad range of pipeline conditions when flowing Prudhoe Bay crude oil. *J. Rheol.* **24**, 603–626.

DALLAS, V., VASSILICOS, J. C. & HEWITT, G. F. 2010 Strong polymer–turbulence interactions in viscoelastic turbulent channel flow. *Phys. Rev. E* **82**, 066303.

DE ANGELIS, E., CASCIOLA, C., L'VOV, V. S., POMYALOV, A., PROCACCIA, I. & TIBERKEVICH, V. 2004 Drag reduction by a linear viscosity profile. *Phys. Rev. E* **70**, 055301.

DEAN, R. B. 1978 Reynolds number dependence of skin friction and other bulk flow variables in two-dimensional rectangular duct flow. *Trans. ASME J. Fluids Engng* **100**, 215–223.

DIMITROPOULOS, C. D., DUBIEF, Y., SHAQFEH, E. S. G., MOIN, P. & LELE, S. K. 2005 Direct numerical simulation of polymer-induced drag reduction in turbulent boundary layer flow. *Phys. Fluids* **17**, 1–4.

DUBIEF, Y., WHITE, C. M., TERRAPON, V. E., SHAQFEH, E. S. G., MOIN, P. & LELE, S. K. 2004 On the coherent drag-reducing and turbulence-enhancing behaviour of polymers in wall flows. *J. Fluid Mech.* **514**, 271–280.

ESCUDIER, M. P., NICKSON, A. & POOLE, R. 2009 Turbulent flow of viscoelastic shear-thinning liquids through a rectangular duct: quantification of turbulence anisotropy. *J. Non-Newtonian Fluid Mech.* **160**, 2–10.

ESCUDIER, M. P., PRESTI, F. & SMITH, S. 1999 Drag reduction in the turbulent pipe flow of polymers. *J. Non-Newtonian Fluid Mech.* **81**, 197–213.

FABULA, A. G. 1971 Fire-fighting benefits of polymeric friction reduction. *Trans ASME J. Basic Engng* **93**, 453–455.

FORREST, F. & GRIERSON, G. A. 1931 Friction losses in cast iron pipe carrying paper stock. *Paper Trade J.* **92**, 39–41.

GOLDA, J. 1986 Hydraulic transport of coal in pipes with drag reducing additives. *Chem. Engng Commun.* **45**, 53–67.

GREENE, H. L., MOSTARDI, R. F. & NOKES, R. F. 1980 Effects of drag reducing polymers on initiation of atherosclerosis. *Polym. Engng Sci.* 20–449.

GYR, A. & TSINOBER, T. 1995 On the rheological nature of drag reduction phenomena. *J. Non-Newtonian Fluid Mech.* **73**, 153–162.

HERSHEY, H. C. & ZAKIN, J. L. 1967 A molecular approach to predicting the onset of drag reduction in the turbulent flow of dilute polymer solutions. *Chem. Engng Sci.* **22**, 184–187.

HOUSIADAS, K. D. & BERIS, A. N. 2003 Polymer-induced drag reduction: effects of the variations in elasticity and inertia in turbulent viscoelastic channel flow. *Phys. Fluids* **15** (8), 2369–2384.

HOUSIADAS, K. D. & BERIS, A. N. 2004 Characteristic scales and drag reduction evaluation in turbulent channel flow of nonconstant viscosity viscoelastic fluids. *Phys. Fluids* **16**, 1581–1586.

HUNT, J. C. R., WRAY, A. A. & MOIN, P. 1988 Eddies, stream, and convergence zones in turbulent flows. In *Center for Turbulence Research – Proceedings of Summer Program Report CTR-S88*, pp. 193–208. Stanford University.

JIMÉNEZ, J. & PINELLI, A. 1999 The autonomous cycle of near-wall turbulence. *J. Fluid Mech.* **389**, 335–359.

JOSEPH, D. D. 1990 *Fluid Dynamics of Viscoelastic Liquids*. Springer.

KALASHNIKOV, V. N. 1998 Dynamical similarity and dimensionless relations for turbulent drag reduction by polymer additives. *J. Non-Newtonian Fluid Mech.* **75**, 209–230.

KIM, J., MOIN, P. & MOSER, R. 1987 Turbulence statistics in fully developed channel flow at low Reynolds number. *J. Fluid Mech.* **177**, 133–166.

KIM, K., ADRIAN, R. J., BALACHANDAR, L. & SURESHKUMAR, R. 2008 Effects of polymer stresses on eddy structures in drag-reduced turbulent channel flow. *Phys. Fluids* **100**, 134504.

KIM, K., LI, C.-F., SURESHKUMAR, R., BALACHANDAR, L. & ADRIAN, R. J. 2007 Effects of polymer stresses on eddy structures in drag-reduced turbulent channel flow. *J. Fluid Mech.* **584**, 281–299.

KRAVCHENKO, A. G., CHOI, H. & MOIN, P. 1993 On the relation of near-wall streamwise vortices to wall skin friction in turbulent boundary layers. *Phys. Fluids* A **5**, 3307–3309.

LUMLEY, J. L. 1969 Drag reduction by additives. *Annu. Rev. Fluid Mech.* **11**, 367–384.

L'VOV, V. S., POMYALOV, A., PROCACCIA, I. & TIBERKEVICH, V. 2004 Drag reduction by polymers in wall bounded turbulence. *Phys. Rev. Lett.* **92**, 244503.

MARTINS, R. S., PEREIRA, A. S., MOMPEAN, G., THAIS, L. & THOMPSON, R. L. 2016 An objective perspective for classic flow classification criteria. *C. R. Méc.* **344**, 52–59.

MERRILL, E. W. & HORN, A. F. 1984 Scission of macromolecules in dilute solution: extensional and turbulent flows. *Polym. Commun.* **25**, 144–146.

MIN, T., YOO, J. Y., CHOI, H. & JOSEPH, D. D. 2003 Drag reduction by polymer additives in a turbulent channel flow. *J. Fluid Mech.* **486**, 213–238.

MOUSSA, T. & TIU, C. 1994 Factors affecting polymer degradation in turbulent pipe flow. *Chem. Engng Sci.* **49**, 1681–1692.

MYSELS, K. J. 1949 Flow of thickened fluids. U.S. Patent 2 Dec. 27 492, 173.

ORLANDI, P. 1996 A tentative approach to the direct simulation of drag reduction by polymers. *J. Non-Newtonian Fluid Mech.* **60**, 277–301.

PATERSON, R. W. & ABERNATHY, F. H. 1970 Turbulent flow drag reduction and degradation with dilute polymer solutions. *J. Fluid Mech.* **43**, 689–710.

PEREIRA, A. S., ANDRADE, R. M. & SOARES, E. J. 2013 Drag reduction induced by flexible and rigid molecules in a turbulent flow into a rotating cylindrical double gap device: comparison between poly (ethylene oxide), polyacrylamide, and xanthan gum. *J. Non-Newtonian Fluid Mech.* **202**, 72–87.

PEREIRA, A. S., MOMPEAN, G., THAIS, L. & SOARES, E. J. 2017 Transient aspects of drag reducing plane couette flows. *J. Non-Newtonian Fluid Mech.* **241**, 60–69.

PEREIRA, A. S. & SOARES, E. J. 2012 Polymer degradation of dilute solutions in turbulent drag reducing flows in a cylindrical double gap rheometer device. *J. Non-Newtonian Fluid Mech.* **179**, 9–22.

PETERLIN, A. 1961 Streaming birefringence of soft linear macromolecules with finite chain length. *Polymer* **2**, 257–291.

PINHO, F. T. & WHITELAW, J. H. 1990 Flow of non-Newtonian fluids in a pipe. *J. Non-Newtonian Fluid Mech.* **34**, 129–144.

PTASINSKI, P. K., NIEUWSTADT, F. T., VAN DEN BRULE, B. H. A. A. & HULSEN, M. A. 2001 Experiments in turbulent pipe flow with polymer additives at maximum drag reduction. *Turbul. Combust.* **66**, 159–182.

RYSKIN, G. 1987 Turbulent drag reduction by polymers: a quantitative theory. *Phys. Rev. Lett.* **59**, 2059–2062.

SELLIN, R. H. J., HOYT, J. W., POLIERT, J. & SCRIVENER, O. 1982 The effect of drag reducing additives on fluid flows and their industrial applications part II: present applications and future proposals. *J. Hydraul Res.* **20**, 235–292.

SEYER, F. A. & METZNER, A. B. 1969 Turbulence phenomena in drag reducing systems. *AIChE J.* **15**, 426–434.

SOARES, E. J., SANDOVAL, G. A. B., SILVEIRA, L., PEREIRA, A. S., TREVELIN, R. & THOMAZ, F. 2015 Loss of efficiency of polymeric drag reducers induced by high Reynolds number flows in tubes with imposed pressure. *Phys. Fluids* **27**, 125105.

SURESHKUMAR, R. & BERIS, A. N. 1995 Effect of artificial stress diffusivity on the stability of numerical calculations and the dynamics of time-dependent viscoelastic flows. *J. Non-Newtonian Fluid Mech.* **60**, 53–80.

SURESHKUMAR, R., BERIS, A. N. & HANDLER, R. A. 1997 Direct numerical simulation of the turbulent channel flow of a polymer solution. *Phys. Fluids* **9**, 743–755.

TABOR, M. & DE GENNES, P. G. 1986 A cascade theory of drag reduction. *Europhys. Lett.* **2**, 519–522.

TERRAPON, V. E., DUBIEF, Y., MOIN, P., SHAQFEH, E. S. G. & LELE, S. K. 2004 Simulated polymer stretch in a turbulent flow using brownian dynamics. *J. Fluid Mech.* **504**, 61–71.

THAIS, L., GATSKI, T. B. & MOMPEAN, G. 2012 Some dynamical features of the turbulent flow of a viscoelastic fluid for reduced drag. *J. Turbul.* **13**, 1–26.

THAIS, L., GATSKI, T. B. & MOMPEAN, G. 2013 Analysis of polymer drag reduction mechanisms from energy budgets. *Intl J. Heat Fluid Flow* **43**, 52–61.

THAIS, L., TEJADA-MARTINEZ, A., GATSKI, T. B. & MOMPEAN, G. 2011 A massively parallel hybrid scheme for direct numerical simulation of turbulent viscoelastic channel flow. *Comput. Fluids* **43**, 134–142.

TOMS, B. A. 1948 Some observations on the flow of linear polymer solutions through straight tubes at large Reynolds numbers. In *Proceedings of the International Congress of Rheology, Holland, North-Holland, Amsterdam, Section II*, pp. 135–141. North-Holland.

DEN TOONDER, J. M. J., NIEUWSTADT, F. T. M. & KUIKEN, G. D. C. 1995 The role of elongational viscosity in the mechanism of drag reduction by polymer additives. *Appl. Sci. Res.* **54**, 95–123.

VIRK, P. S. 1975 Drag reduction fundamentals. *AIChE J.* **21**, 625–656.

VIRK, P. S., MICKLEY, H. S. & SMITH, K. A. 1967 The Toms phenomenon: turbulent pipe flow of dilute polymer solutions. *J. Fluid Mech.* **22**, 22–30.

VIRK, P. S., MICKLEY, H. S. & SMITH, K. A. 1970 The ultimate asymptote and mean flow structure in Toms' phenomenon. *Trans. ASME J. Appl. Mech.* **37**, 488–493.

WARHOLIC, M. D., MASSAH, H. & HANRATTY, T. J. 1999 Influence of drag-reducing polymers on turbulence: effects of Reynolds number, concentration and mixing. *Exp. Fluids* **27**, 461–472.

WEI, T. & WILLMARTH, W. W. 1992 Modifying turbulent structure with drag-reducing polymer additives in turbulent channel flows. *J. Fluid Mech.* **245**, 619–641.

WHITE, C. M., DUBIEF, Y. & KLEWICKI, J. 2012 Re-examining the logarithmic dependence of the mean velocity distribution in polymer drag reduced wall-bounded flow. *Phys. Fluids* **24**, 021701.

WHITE, C. M. & MUNGAL, M. G. 2008 Mechanics and prediction of turbulent drag reduction with polymer additives. *Annu. Rev. Fluid Mech.* **40**, 235–256.

WHITE, C. M., SOMANDEPALLI, V. S. R. & MUNGAL, M. G. 2004 The turbulence structure of drag-reduced boundary layer flow. *Exp. Fluids* **36**, 62–69.